International Journal of Solids and Structures 163 (2019) 194–210

Contents lists available at ScienceDirect

International Journal of Solids and Structures

journal homepage: www.elsevier.com/locate/ijsolstr

Failure characterization of solid structures based on an equivalence of cohesive zone model

Hao Long[a,c], Lihong Liang[a,c,*], Yueguang Wei[b,*]

[a] LNM, Institute of Mechanics, Chinese Academy of Sciences, Beijing 100190, China
[b] College of Engineering, Peking University, Beijing 100871, China
[c] School of Engineering Science, University of Chinese Academy of Sciences, Beijing 100049, China

ARTICLE INFO

Article history:
Received 3 July 2018
Revised 19 November 2018
Available online 7 January 2019

Keywords:
Interface cohesive elements
Stiffness
Failure
Thickness effect

ABSTRACT

Cohesive zone models have been widely used to model interface crack initiation and propagation both in single-material media and bi-material systems. For single-material media with cohesive elements inserted into interface among segments, in order to ensure that the introduction of interface cohesive zone models does not affect the mechanical properties of single-material media before the softening stage of cohesive zone models, a selection criterion of stiffness of cohesive elements is proposed theoretically firstly based on the properties' equivalence. Taking the softening stage into account, the mechanical responses of the overall stress-strain relationship of single-material media, for the cases of stable increase of strain and snap-back instability of strain, are both obtained, and the related energy mechanism are investigated. For bi-material systems with cohesive elements at interface between two materials, the thickness-dependent failure characteristics of systems in uniaxial tension are found, which is attributed to the difference of the releasing rate of elastic strain energy in the materials with different thicknesses. Furthermore, as a more complex application of cohesive elements, based on the selection criterion proposed, failure behaviors of the ceramic coating/substrate systems under three-point bending are modeled by finite element method and inserting cohesive elements into the coating segments and the coating/substrate interface simultaneously. The simulation results indicate the transition of dominated failure mode from coating cracking to interface delamination with increasing coating thickness, and show faster damage of thick coating systems, agreeing with experimental results. The effects of interface strength and toughness of cohesive elements on failure are also revealed. These results can provide guidance for the application of cohesive elements, and help us better understand the overall failure behaviors of interface systems.

1. Introduction

Cohesive zone models (CZMs) have been widely used to predict the initiation and propagation of cracks. The concept of cohesive fracture was proposed by Barenblatt (1959, 1962) who assumed in a narrow region ahead of the crack tip, the opposite surfaces are hold together by cohesive forces. Consequently, the stress singularity of the crack tip is removed. If the distributed cohesive forces are constant and equal to the yield stress, this concept actually refers to the Dugdale's strip yield model (Dugdale, 1960). Afterwards, a large variety of cohesive zone laws have been proposed by defining the traction-separation relationship, such as polynomial (Tvergaard, 1990), piecewise linear (Tvergaard and Hutchinson, 1992), exponential (Xu and Needleman, 1993) and bilinear (Camanho et al., 2003) cohesive zone laws. The CZMs gradually become a popular tool in finite element method (FEM) and are often to be used to simulate fracture behaviors. The CZMs can not only be used to model cracks within single-material media, such as coating cracking of coating/substrate systems (Abdul-Baqi and Van der Giessen, 2002; Białas et al., 2005; Li et al., 2014) and matrix cracking of composite materials (Kumar et al., 2015; Shi and Soutis, 2016), but also be used to investigate interface delamination of bi-material systems, such as delamination of composite materials (Airoldi et al., 2015; Cameselle-Molares et al., 2018; Zou et al., 2003), adhesive joints (Lelias et al., 2015; Neumayer et al., 2016) and some other layered structures (Peng and Wei, 2016).

Two basic approaches have been proposed to implement finite element simulations with CZMs (Kubair and Geubelle, 2003; Vocialta et al., 2017): intrinsic and extrinsic. In the intrinsic approach (Xu and Needleman, 1994), the cohesive zone law is taken to be initially elastic and the cohesive elements are placed along the potential crack path at the beginning of the simulation. This approach allows easy and straightforward implementation, but its draw-

* Corresponding authors.
E-mail addresses: lianglh@lnm.imech.ac.cn (L. Liang), weiyg@pku.edu.cn (Y. Wei).

https://doi.org/10.1016/j.ijsolstr.2019.01.008
0020-7683/

back is the introduction of artificial compliance (Klein et al., 2001; Tomar et al., 2004), which leads to the decrease of wave speed for dynamic crack propagation problems (Tabiei and Zhang, 2017). As for the extrinsic approach (Camacho and Ortiz, 1996), the cohesive zone law is taken to be initially rigid, and thus the artificial compliance is avoided (Falk et al., 2001). However, considering that the cohesive elements are inserted progressively as required during the simulation involving local mesh modification and node duplication, the extrinsic approach is challenging both in its serial and parallel implementation (Vocialta et al., 2017).

Since the intrinsic approach allows convenient implementation and has been widely adopted in previous studies, what we are concerned about is the intrinsic approach. As the intrinsic cohesive elements, which are analogous to a series of springs, are inserted into the single-material media, the system becomes discrete, and the situation is naturally different from the standard continuum mechanics. But before the damage initiation (i.e., the traction stress reaches its strength), the overall equivalent elastic constants should remain unchanged before and after the CZMs are inserted. Thus, we aim to propose an approach to ensure the equivalence of intrinsic CZMs. It is noteworthy that when zero-thickness cohesive elements, which are mostly focused on by studies involving the intrinsic approach, are inserted to all continuum element boundaries to allow arbitrary crack paths (Xu and Needleman, 1994), the reduction of equivalent Young's modulus becomes significant as the density of cohesive elements increases (Klein et al., 2001). Nevertheless, the element size should be small enough to capture the stress distribution accurately inside the cohesive zone ahead of the crack tip (Tomar et al., 2004; Turon et al., 2007). A straight way to get rid of the artificial compliance is to increase the initial stiffness of CZMs. When it comes to the bilinear cohesive zone law, Camanho et al. (2003) called k penalty stiffness and a high initial stiffness should be used to hold the adjacent faces together. Afterwards, Turon et al. (2007) pointed out that $k \gg E/t$, where E and t are the Young's modulus and the thickness of surrounding material connected by CZMs, respectively. However, large values of stiffness can only ensure that the introduced fictitious compliance is small (Blal et al., 2012; Turon et al., 2007), and they may cause oscillations of tractions (Schellekens and de Borst, 1993) and convergence problems. Some other approaches such as introducing some constraints (Zhang and Chen, 2015) are quite similar to the extrinsic approach. Therefore, for intrinsic CZMs with initially elastic cohesive law, an efficient approach to ensure the equivalence of single-material inserted with CZMs to the original is still lacking.

Apart from the equivalence of CZMs before damage initiation, the accurate acquisition of the traction-separation relationship of CZMs is also essential to the failure characterization of solid structures. The relationship can be directly determined from experiments by using the Digital Image Correlation (DIC) technique (Abanto-Bueno and Lambros, 2005; Tan et al., 2005), and experiments calibrated with finite element simulations (Alfano et al., 2008; Lee et al., 2010) or other independent experiments (Ferracin et al., 2003). On the other hand, parameters of phenomenological CZMs can also be extracted from atomistic simulations (Choi and Kim, 2007; Yamakov et al., 2006), especially for microscale and nanoscale cohesive laws. In order to obtain a convergent and intrinsic interfacial cohesive law, models with different thicknesses were investigated, and the overall failure of interface structures such as Al/Si systems (Gall et al., 2000) and Ag/MgO systems (You et al., 2018) shows a thickness-dependent characteristic. A theoretic explanation of this characteristic can shed light on the better understanding of the overall mechanical responses when we attempt to extract interfacial cohesive parameters by means of atomistic simulations.

The remainder of this paper is organized as follows. Section 2 gives a brief introduction to CZMs. In Section 3, in order to ensure the introduction of CZMs does not affect the mechanical properties of single-material media before crack propagation, a criterion of selecting the stiffness of finite-thickness cohesive elements is proposed based on a series model. And then, considering the softening stages of CZMs, the overall mechanical responses such as stress-strain relationship are studied. Section 4 focuses on a theoretic explanation of the thickness-dependent failure characteristic of bi-material systems with cohesive elements at interface. Since the failure of complex systems is always the mixture of single-material cracking and interface delamination (Abdul-Baqi and Van der Giessen, 2002; Li et al., 2014), cohesive elements should be inserted into the single-material media and the interface simultaneously. Thus, as an example, failure behaviors of ceramic coating/substrate systems under three-point bending are simulated based on FEM in Section 5. Finally, the relevant conclusions are summarized in Section 6.

2. Cohesive zone model

The cohesive zone model with bilinear separation-traction law is discussed in this paper. There are three different basic modes of loading involving different crack displacements (Hertzberg, 1996): mode I (opening or tensile mode), mode II (sliding or in-plane shear mode) and mode III (tearing or anti-plane shear mode). Correspondingly, the bilinear separation-traction law (Camanho et al., 2003) for pure Mode I and pure mode II or mode III loading is shown in Fig. 1(a) and (b), respectively.

Except for the case of $\delta_n < 0$, the bilinear traction-separation law can be expressed as

$$\sigma_i = \begin{cases} k_i\delta_i, \delta_i < \delta_i^0 \\ \dfrac{\delta_i^f - \delta_i}{\delta_i^f - \delta_i^0}\sigma_i^0, \delta_i^0 \le \delta_i < \delta_i^f \\ 0, \delta_i \ge \delta_i^f \end{cases} (i = n,t,s) \tag{1}$$

where σ is traction stress, δ is separation (displacement) and k is stiffness. Subscripts n, t, and s represent the normal direction (Mode I), the first tangential direction (Mode II), and the second tangential direction (Mode III), respectively. Superscripts 0 and f represent the damage initiation point and the fracture point, respectively. As shown in Fig. 1, at the damage initiation point, the traction reaches its maximum, i.e., the strength σ^0, and corresponding separation is the critical displacement δ^0. After a softening stage, the stress reduces to zero, and separation reaches the fracture displacement δ_f. The area under the traction-separation curve is the respective fracture toughness:

$$\Gamma_i = \int_0^{\delta_i^f} \sigma_i \mathrm{d}\delta_i = \frac{1}{2}\sigma_i^0\delta_i^0, i = n,t,s \tag{2}$$

For the case of $\delta_n < 0$, the following condition is introduced to avoid interpenetration of the crack interfaces (Camanho et al., 2003):

$$\sigma_n = k_n\delta_n, \delta_n < 0 \tag{3}$$

Under mix-mode loading, damage may initiate before one stress component reaches its tolerance. Therefore, the quadratic nominal stress criterion (Cui et al., 1992) for damage initiation is adopted here:

$$\left(\frac{<\sigma_n>}{\sigma_n^0}\right)^2 + \left(\frac{\sigma_t}{\sigma_t^0}\right)^2 + \left(\frac{\sigma_s}{\sigma_s^0}\right)^2 = 1 \tag{4}$$

Then, the power law criterion (Camanho et al., 2003; Dassault Systèmes, 2014) to predict crack propagation is used:

$$\left(\frac{G_n'}{\Gamma_n}\right)^\alpha + \left(\frac{G_t'}{\Gamma_t}\right)^\alpha + \left(\frac{G_s'}{\Gamma_s}\right)^\alpha = 1 \tag{5}$$

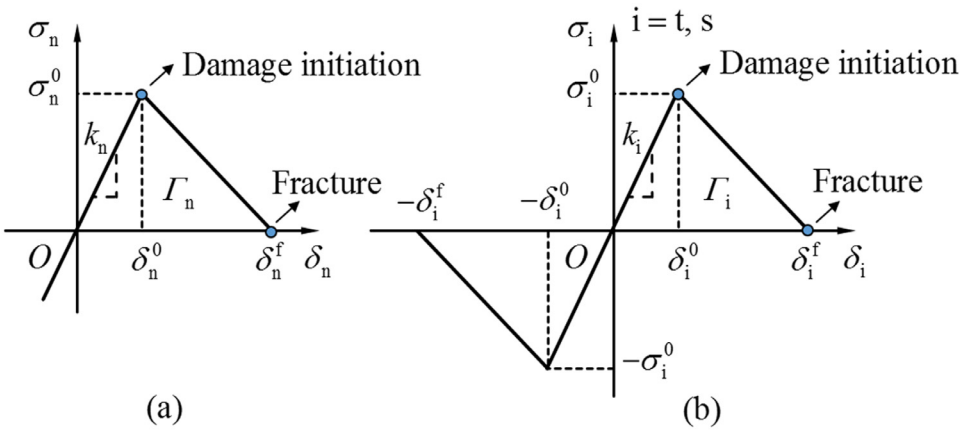

Fig. 1. Bilinear separation-traction law (a) for pure mode I loading, and (b) for pure mode II or mode III loading.

where G' is the work done by traction stress and Γ is the fracture toughness. The power law exponent is chosen to be $\alpha = 1$.

3. Single-material media with inserted cohesive elements

3.1. Selection criterion of stiffness of cohesive elements

3.1.1. Theoretical analysis based on a series model

The artificial compliance problem of zero-thickness cohesive elements has been clarified by means of 1D theoretical analysis in a lot of literature (Blal et al., 2012; Klein et al., 2001; Tabiei and Zhang, 2017; Turon et al., 2007). In order to eliminate the artificial compliance, i.e., ensure that the insertion of intrinsic cohesive elements does not affect the original mechanical properties of single-material media before crack propagation, an effective approach is proposed based on a series model in this section. This approach actually is converted to a selection criterion of stiffness of finite-thickness cohesive elements. Here, we consider cohesive elements have a small thickness t_0, which is not incorporated in the bilinear cohesive zone law.

The following discussion is limited in small deformation and linear elasticity. And the softening stage of cohesive elements is not considered. In order to express the generality of the criterion, the three-dimensional case is discussed and there are four independent parameters: t_0, k_n, k_t and k_s.

Here, the single-material medium called matrix material is assumed to be homogeneous and isotropic. Its Young's modulus and Poisson's ratio are E_m and ν_m, respectively. Fig. 2(a) shows a piece of matrix material with width of B and height of H. Many equal spacing layers of cohesive elements with thickness of t_0 are inserted along the x direction, as shown in Fig. 2(b).

The discrete system composed of matrix material and cohesive elements can be equivalent to a continuous medium. In order to ensure that the insertion of cohesive elements does not affect original mechanical properties, the elastic constants of the equivalent continuous medium should be equal to those of the matrix material correspondingly, from which the selection criterion of stiffness can be obtained.

To obtain the equivalent elastic constants, we consider the system is in three basic loading modes, including uniaxial tension and in-plane shear and anti-plane shear. Since the stress states in all these cases are uniform, the following analysis is independent of the number of cohesive elements. Furthermore, a representative volume element (RVE) can be selected whether the system is in tension or in shear, as shown in Fig. 2(c) and (d).

Due to the introduction of cohesive elements, the length of the RVE increases from L to$L' = L + t_0$, implying the increase of the overall volume. If we let $t_0 = 0$, the finite-thickness cohesive elements reduce to zero-thickness cohesive elements and the overall volume remains unchanged.

Firstly, we consider the system in uniaxial tension, i.e., pure mode I loading. As shown in Fig. 2(c), the RVE is subjected to uniform tensile stress at the boundaries. In this series model, the elongation of the RVE can be divided into two parts: elongation of the matrix material and elongation of cohesive elements. Thus, the normal strain of the RVE in the x direction can be expressed as

$$\varepsilon_{xx} = \frac{\Delta L'}{L'} = \frac{1}{L + t_0}\left(\frac{\sigma_{xx} L}{E_m} + \frac{\sigma_{xx}}{k_n}\right) = \frac{\sigma_{xx}}{E_{eq}} \tag{6}$$

where E_{eq} is the equivalent Young's modulus. Then it can be derived as

$$E_{\mathrm{eq}} = E_{\mathrm{m}} \frac{1 + t_0/L}{1 + E_{\mathrm{m}}/(k_{\mathrm{n}} L)} \tag{7}$$

where t_0/L and $E_m/(k_n L)$ are two dimensionless parameters. t_0/L represents the relative volume change of the RVE due to the introduction of cohesive elements. And $E_m/(k_n L)$ denotes the relative stiffness of the matrix material compared with that of cohesive elements. Since it is required that $E_{\mathrm{eq}} = E_m$, we obtain

$$k_{\mathrm{n}} t_0 = E_{\mathrm{m}} \tag{8}$$

It should be noted that Eq. (8) can be rewritten in the form of the ratio of two lengths: $t_0/\delta_n^0 = E_m/\sigma_n^0$. Since the ratio of strength and Young's modulus is about $E_{\mathrm{m}}/\sigma_{\mathrm{n}}^0 \approx 10^2 \sim 10^3$, the thickness of cohesive elements is two or three orders of magnitude larger than the critical displacement.

If we consider cohesive elements as a special material, the normal strain is given by $(\varepsilon_{xx})_{\mathrm{CE}} = \sigma_{xx}/(k_n t_0)$. Thus, the Young's modulus of cohesive elements can be defined by $E_{\mathrm{CE}} = k_n t_0$. Consequently, Eq. (8) can be written as $E_{\mathrm{CE}} = E_{\mathrm{m}}$, i.e., the Young's modulus of cohesive elements is equivalent to that of the matrix.

When the system is in uniaxial tension, the equivalent Poisson's ratio ν_{eq} and the equivalent bulk modulus K_{eq} of the RVE can be obtained. Considering that the lateral shrinkage of cohesive elements always follows that of the matrix material passively, the equivalence of Poisson's ratio and bulk modulus are naturally satisfied, i.e., $\nu_{\mathrm{eq}} = \nu_{\mathrm{m}}$ and $K_{\mathrm{eq}} = K_{\mathrm{m}}$. Detailed analysis is given in Appendix A.

Next, we consider the system in in-plane shear, i.e., pure mode II loading. As shown in Fig. 2(d), the RVE is subjected to uniform shear stress τ_{xy} at the boundaries. The vertical displacement

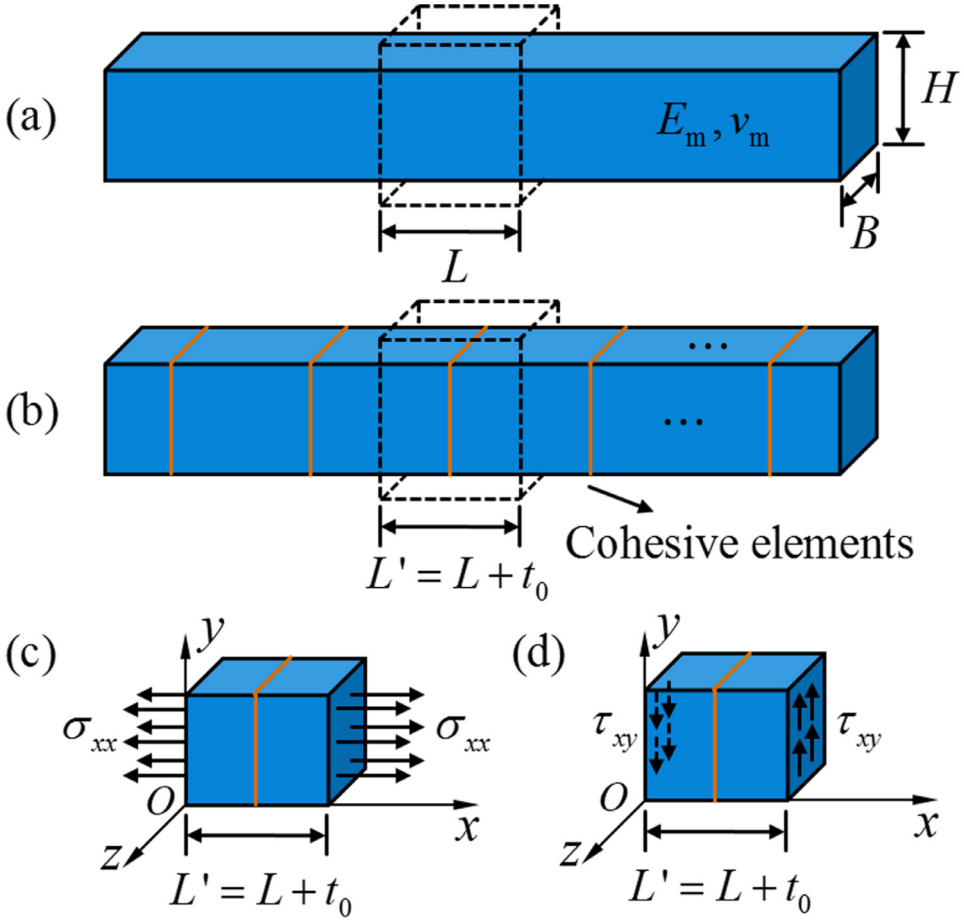

Fig. 2. (a) A piece of matrix material; (b) the system composed of matrix material and cohesive elements; (c) the representative volume element (RVE) in uniaxial tension; (d) the RVE in shear.

of right boundary ($x = L'$) relative to the left boundary ($x = 0$) is denoted by $\bar{v}$. Then, the engineering shear strain γ_{xy} can be expressed as

$$\gamma_{xy} = \frac{\bar{v}}{L'} = \frac{1}{L + t_0}\left(\frac{\tau_{xy} L}{G_m} + \frac{\tau_{xy}}{k_t}\right) = \frac{\tau_{xy}}{G_{eq}} \tag{9}$$

where G_{eq} is the equivalent shear modulus. Then it can be derived as

$$G_{eq} = G_m \frac{1 + t_0/L}{1 + G_m/(k_t L)} \tag{10}$$

Since it is required that $G_{eq} = G_m$, we obtain

$$k_t t_0 = G_m \tag{11}$$

If we consider cohesive elements as a special material, the shear strain is given by $(\gamma_{xy})_{CE} = \tau_{xy}/(k_t t_0)$. Thus, the shear modulus of cohesive elements can be defined by $G_{CE} = k_t t_0$. Consequently, Eq. (11) can be written as $G_{CE} = G_m$, i.e., the shear modulus of cohesive elements is equivalent to that of the matrix.

At last, we consider the system in pure mode III loading. The RVE is subjected to uniform shear stress τ_{xz} at the boundaries. The stiffness k_s can be obtained by similar analysis:

$$k_s t_0 = G_m \tag{12}$$

To ensure that the equivalent elastic constants are equal to those of matrix material correspondingly, i.e., $E_{eq} = E_m$, $\nu_{eq} = \nu_m$ (or $K_{eq} = K_m$) and $G_{eq} = G_m$, Eqs. (8), (11) and (12) are obtained. Noting that the matrix material is isotropic, substitution of $G_m = E_m/[2(1 + \nu_m)]$ in Eqs. (11) and (12) yields

$$\begin{cases} k_n t_0 = E_m \\ k_t = \dfrac{1}{2(1 + \nu_m)} k_n \\ k_s = \dfrac{1}{2(1 + \nu_m)} k_n \end{cases} \tag{13}$$

This is the selection criterion of stiffness of cohesive elements for three-dimensional case. There are four parameters of cohesive elements (t_0, k_n, k_t, k_s) in Eq. (13). But only three conditions are given. One of these parameters should be selected as a free parameter, for example, the thickness of cohesive elements t_0. If the volume change due to the introduction of cohesive elements brings additional effects, for instance, the increase of span length of beam structure, we should ensure that the relative volume change is as small as possible, i.e., $t_0/L \ll 1$. In addition, the spacing L represents the continuum element size if cohesive elements are inserted to all continuum element boundaries. Usually selection of L value should be much larger than t_0. According to the present analysis, when $t_0/L < 0.1$, the result should be mesh-independent.

In the case of plane stress, k_s should not appear and Eq. (13) reduces to

$$\begin{cases} k_n t_0 = E_m \\ k_t = \dfrac{1}{2(1 + \nu_m)} k_n \end{cases} \tag{14}$$

In the case of plane strain, replacing E_m and ν_m with $E_m = E_m/(1 - \nu_m^2)$ and $\nu_m = \nu_m/(1 - \nu_m)$ respectively in Eq. (14),

we can obtain

$$\begin{cases} k_n t_0 = \dfrac{E_m}{1-\nu_m{}^2} \\ k_t = \dfrac{1-\nu_m}{2} k_n \end{cases} \tag{15}$$

If we let $t_0 = 0$, finite-thickness cohesive elements reduce to zero-thickness cohesive elements. Eqs. (7), (A.3) and (10) reduce to

$$\begin{cases} E_{eq} = E_m \dfrac{1}{1+E_m/(k_n L)} \\ \nu_{eq} = \nu_m \dfrac{1}{1+E_m/(k_n L)} \\ G_{eq} = G_m \dfrac{1}{1+G_m/(k_t L)} \end{cases} \tag{16}$$

Thus, when zero-thickness cohesive elements are inserted, the CZMs introduce a fictitious compliance and the equivalent elastic constants are always less than those of the matrix material correspondingly, i.e., $E_{eq} < E_m$, $\nu_{eq} < \nu_m$ and $G_{eq} < G_m$. To minimize the fictitious compliance, large values of stiffness should be selected, i.e., $k_n \gg E_m/L$, $k_t \gg G_m/L$. These results agree with that Turon et al. (2007) proposed. On the other hand, if zero-thickness cohesive elements are inserted to all continuum element boundaries, L represents the continuum element size. Thus from Eq. (16), the equivalent or effective elastic constants are mesh-dependent. And when stiffness k_i (i = n, t, s) or element size L tends to infinity, the equivalent elastic constants are towards those of matrix material correspondingly. This is similar to that Klein et al. (2001) pointed out.

3.1.2. Numerical verification

In order to further validate the selection criterion of stiffness of cohesive elements, we take the RVE in uniaxial tension under plane stress state as an example to perform simulations based on FEM.

In the simulations, dimensionless analysis was carried out with the equivalent Young's modulus E_{eq} and Poisson's ratio ν_{eq} being expressed by

$$\begin{cases} \dfrac{E_{eq}}{E_m} = f_1\left(\dfrac{H}{L}, \dfrac{k_n L}{E_m}, \nu_m\right) \\ \dfrac{\nu_{eq}}{\nu_m} = f_2\left(\dfrac{H}{L}, \dfrac{k_n L}{E_m}, \nu_m\right) \end{cases} \tag{17}$$

A series of values of the parameter $k_n L/E_m$ are selected to investigate its influence. Other dimensionless parameters are fixed at $H/L = 0.5$ and $\nu_m = 0.2$. It should be noted that the thickness of cohesive elements t_0 is not an independent parameter since it is selected according to Eq. (14). Zero-thickness cohesive elements are also considered for comparison.

As shown in Fig. 3(a) and (b), the theoretical predictions and simulation results based on FEM match well: under the selection criterion of stiffness of finite-thickness cohesive elements proposed, the equivalent Young's modulus and the equivalent Poisson's ratio are equal to those of matrix material correspondingly. Compared to zero-thickness cohesive elements, the advantage of finite-thickness cohesive elements is that no artificial compliance is introduced without necessity of large values of stiffness of cohesive elements. However, how to deal with possible additional effects due to the increase of overall volume is a new problem. If there is no obvious additional effect, finite-thickness cohesive elements should be preferred.

In the above analysis, we can assume $L' = L$ as well, which means that the overall volume remains unchanged but the volume of matrix material reduces. The same selection criterion of stiffness of cohesive elements can be obtained.

3.2. The overall mechanical responses

Taking into account the softening stage of cohesive elements, the overall mechanical responses can be obtained. Based on the 1D series model, the overall responses have been discussed based on polynomial (Chaboche et al., 2001), exponential (Gao and Bower, 2004) and bilinear (Hamitouche et al., 2008; Needleman, 2014) cohesive law in the linear-elastic situation. The elastic-plastic situation based on the bilinear cohesive law have also been discussed by Yu et al. (2016). It should be noted that the equivalence of CZMs was not considered in these studies and most of them mainly focused on the techniques to overcome convergence problems caused by snap-back instability. Here, based on the selection criterion proposed in Section 3.1, we consider the overall stress-strain relationship and interface separation-overall strain relationship again, with the corresponding energy analysis in the whole process.

As an example, the RVE in uniaxial tension is considered here. As illustrated in Fig. 2(c), the normal strain of the RVE in the x direction can be expressed by

$$\varepsilon_{xx} = \frac{\Delta L'}{L'} = \frac{1}{L+t_0}\left(\frac{\sigma_{xx} L}{E_m} + \delta_n\right) \tag{18}$$

Considering $\sigma_{xx} = \sigma_n$ in the series model, we can eliminate δ_n in Eq. (18) by substituting Eq. (1). Then, the overall stress-strain relationship simplified by utilizing $E_m = k_n t_0$ is given by

$$\frac{\sigma_{xx}}{\sigma_n^0} = \begin{cases} \dfrac{E_m}{\sigma_n^0}\varepsilon_{xx}, & \varepsilon_{xx} < \dfrac{\sigma_n^0}{E_m} \\ \dfrac{(1+\Lambda)\Lambda_{cr}}{\Lambda_{cr}-\Lambda}\dfrac{E_m}{\sigma_n^0}\varepsilon_{xx} & \\ \quad -\dfrac{(1+\Lambda_{cr})\Lambda}{\Lambda_{cr}-\Lambda}, & \min\left\{\dfrac{\sigma_n^0}{E_m}, \dfrac{(1+\Lambda_{cr})\Lambda}{(1+\Lambda)\Lambda_{cr}}\dfrac{\sigma_n^0}{E_m}\right\} \le \varepsilon_{xx} \\ & < \max\left\{\dfrac{\sigma_n^0}{E_m}, \dfrac{(1+\Lambda_{cr})\Lambda}{(1+\Lambda)\Lambda_{cr}}\dfrac{\sigma_n^0}{E_m}\right\} \\ 0, & \varepsilon_{xx} \ge \dfrac{(1+\Lambda_{cr})\Lambda}{(1+\Lambda)\Lambda_{cr}}\dfrac{\sigma_n^0}{E_m} \end{cases} \tag{19}$$

where Λ and Λ_{cr} are two dimensionless quantities:

$$\Lambda = \frac{t_0}{L} = \frac{E_m}{k_n L} = \frac{E_m}{\sigma_n^0}\frac{\delta_n^0}{L}, \Lambda_{cr} = \frac{\delta_n^0}{\delta_n^f - \delta_n^0} \tag{20}$$

It can be seen that Λ represents the relative change of overall volume due to the insertion of cohesive elements, or the relative stiffness of matrix material compared with that of cohesive elements. Λ_{cr} is a function of δ_n^f/δ_n^0 and it is a critical value of Λ as suggested by Hamitouche et al. (2008). The maximum between σ_n^0/E_m and $(1+\Lambda_{cr})\Lambda\sigma_n^0/[(1+\Lambda)\Lambda_{cr}E_m]$ in Eq. (19) relies on the relative magnitude of Λ and Λ_{cr}.

Taking Eq. (1) into Eq. (19), σ_{xx} can be eliminated and the relationship between separation and the overall strain can be obtained:

$$\frac{\delta_n}{\delta_n^0} = \begin{cases} \dfrac{E_m}{\sigma_n^0}\varepsilon_{xx}, & \varepsilon_{xx} < \dfrac{\sigma_n^0}{E_m} \\ \dfrac{1+\Lambda_{cr}}{\Lambda_{cr}-\Lambda} - \dfrac{1+\Lambda}{\Lambda_{cr}-\Lambda}\dfrac{E_m}{\sigma_n^0}\varepsilon_{xx}, & \min\left\{\dfrac{\sigma_n^0}{E_m}, \dfrac{(1+\Lambda_{cr})\Lambda}{(1+\Lambda)\Lambda_{cr}}\dfrac{\sigma_n^0}{E_m}\right\} \le \varepsilon_{xx} \\ & < \left\{\dfrac{\sigma_n^0}{E_m}, \dfrac{(1+\Lambda_{cr})\Lambda}{(1+\Lambda)\Lambda_{cr}}\dfrac{\sigma_n^0}{E_m}\right\} \\ \dfrac{1+\Lambda}{\Lambda}\dfrac{E_m}{\sigma_n^0}\varepsilon_{xx}, & \varepsilon_{xx} \ge \dfrac{(1+\Lambda_{cr})\Lambda}{(1+\Lambda)\Lambda_{cr}}\dfrac{\sigma_n^0}{E_m} \end{cases} \tag{21}$$

Similar to the bilinear traction-separation law, the overall stress-strain relationship and separation-strain relationship are

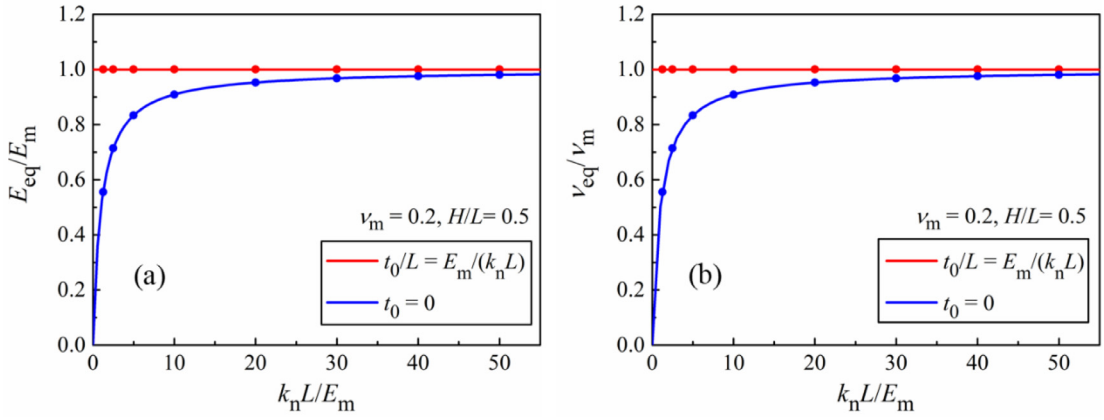

Fig. 3. Influences of stiffness of cohesive elements on (a) the equivalent Young's modulus E_{eq} and (b) the equivalent Poisson's ratio ν_{eq}. The solid lines are theoretical results based on Eqs. (7) and (A.3), and the symbols are simulation results based on FEM.

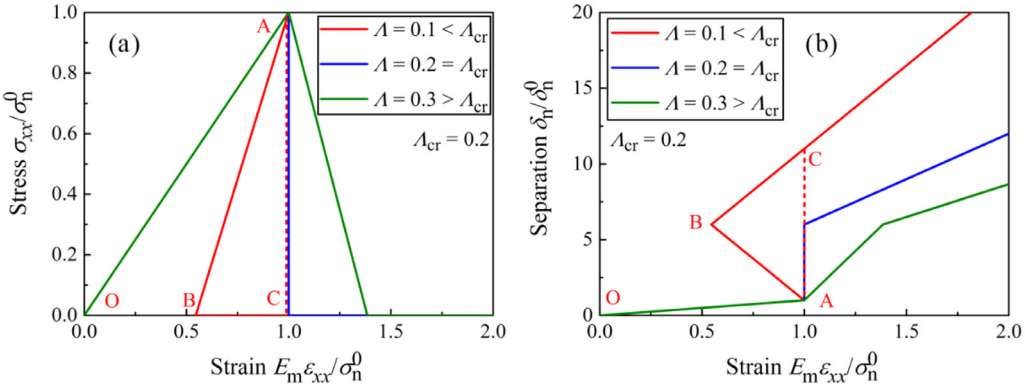

Fig. 4. (a) The overall stress-strain relationship, and (b) the interface separation-overall strain relationship of the RVE for several values of Λ and fixed $\Lambda_{cr} = 0.2$.

piecewise linear functions. From Eqs. (19) and (21), if we normalize the strain with σ_n^0/E_m, both the stress-strain relationship and the separation-strain relationship are functions of Λ and Λ_{cr} only.

When Λ_{cr} is fixed at 0.2, the overall stress-strain curves and separation-strain curves for several values of Λ are shown in Fig. 4(a) and (b), respectively. From Eq. (20), different values of Λ can be obtained by changing the parameters of matrix such as E_m and L, while the parameters of cohesive elements remain fixed. Since we have ensured that the equivalent Young's modulus is equal to that of the matrix, curves for different values of Λ are coincident in the elastic stages ($\varepsilon_{xx} \le \sigma_n^0/E_m$), which is more reasonable than results in previous literature (Gao and Bower, 2004; Hamitouche et al., 2008).

The relative magnitude of Λ and Λ_{cr} determines the stability of the system. For $\Lambda = 0.3 > \Lambda_{cr}$, the system is stable. Both the stress and the interface separation are single-valued functions of the overall strain. When the normalized overall strain is $E_m\varepsilon_{xx}/\sigma_n^0 = 1.0$, we have $\sigma_{xx}/\sigma_n^0 = 1.0$ and $\delta_n/\delta_n^0 = 1.0$. Afterwards, the cohesive elements enter the softening stage: the interface separation δ_n increases continuously but the stress decreases. Meanwhile, the elastic deformation in the matrix is released due to the decrease of stress. When $E_m\varepsilon_{xx}/\sigma_n^0 \approx 1.4$, the stress reduces to zero and the separation reaches the fracture displacement. Consequently, fracture occurs and the matrix is completely unloaded.

The case of $\Lambda = \Lambda_{cr} = 0.2$ is a critical state. When the normalized overall strain reaches $E_m\varepsilon_{xx}/\sigma_n^0 = 1.0$, the stress drops abruptly to zero and the separation increases rapidly to δ_n^f. The fracture shows a typical catastrophic characteristic, i.e., an infinite small increment of overall strain will lead to a finite response of the damage (Hao et al., 2010).

For $\Lambda = 0.1 < \Lambda_{cr}$, the system is unstable when the normalized overall strain reaches $E_m\varepsilon_{xx}/\sigma_n^0 = 1.0$. If the system is loaded by progressively increasing the overall strain, the responses of the system will follow the path AC, as the red dashed lines shown in Fig. 4. Then a sudden drop in stress and a corresponding jump in separation will occur. However, path AC is not realistic since it is not incorporated in the solution. If the system is unloaded, there are two possible paths: path AO corresponding to the elastic unloading (the decrease of separation) and path AB corresponding to the continuous increase of separation. Only when path AB is followed, the fracture of cohesive elements will occur eventually. This phenomenon that the overall strain decreases following path AB is called snap-back instability.

The snap-back instability can be explained by energy analysis. The total energy U_T, i.e., the work done by external forces, is calculated by $U_T = \int_0^{\varepsilon_{xx}} \sigma_{xx} d\varepsilon_{xx} \cdot L'$. It should be noted that the energies involved here refer to energies per unit area. And it can be seen that the increase of overall strain corresponds to the increase of the external work. According to energy conservation, the total energy includes two parts: the interface dissipation energy consumed by cohesive elements U_I and the elastic strain energy stored in the matrix U_E.

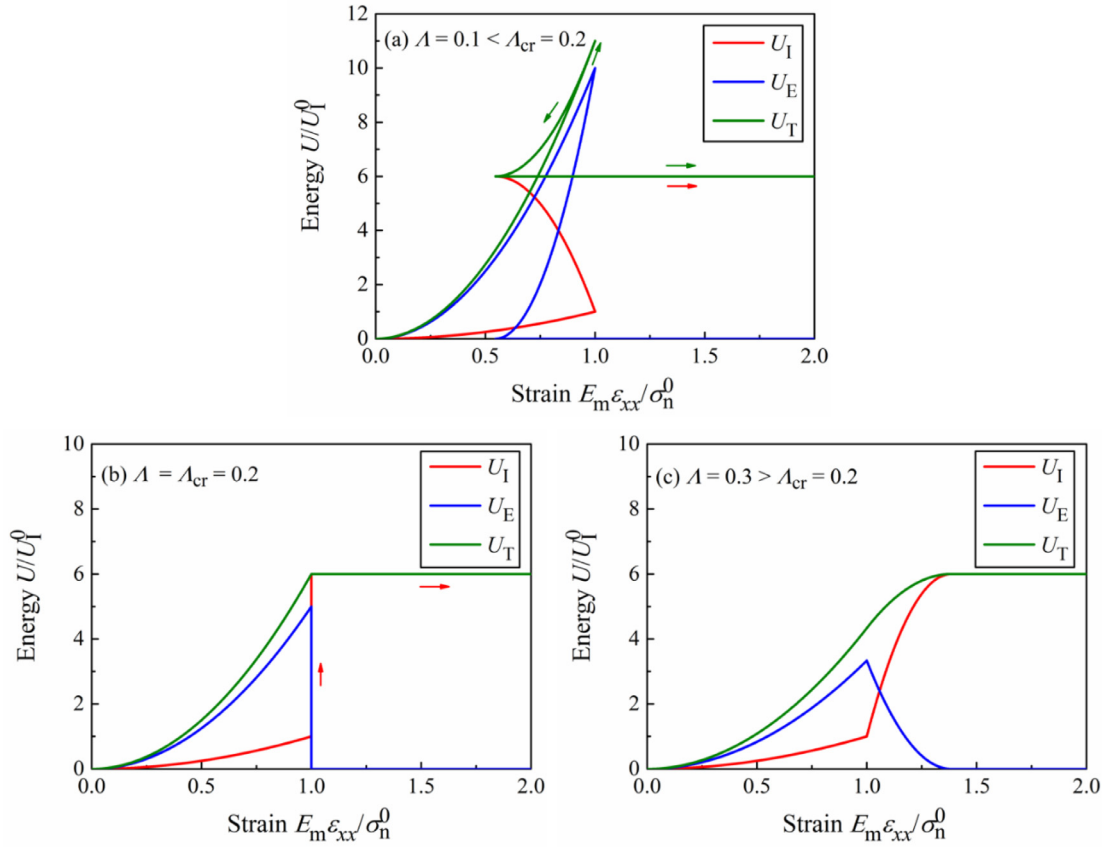

Fig. 5. The external work U_T, the interface dissipation energy U_I, and the elastic strain energy U_E versus the overall strain for fixed $\Lambda_{cr} = 0.2$ and different values of Λ: (a) $\Lambda = 0.1$; (b) $\Lambda = 0.2$; (c) $\Lambda = 0.3$.

The interface dissipation energy is calculated by $U_I = \int_0^{\delta_n} \sigma_n d\delta_n$, and it can be expressed by

$$\frac{U_I}{U_I^0} = \begin{cases} \left[\dfrac{\sigma_{xx}(\varepsilon_{xx})}{\sigma_n^0}\right]^2, & \varepsilon_{xx} < \dfrac{\sigma_n^0}{E_m} \\ \dfrac{1+\Lambda_{cr}}{\Lambda_{cr}} - \dfrac{1}{\Lambda_{cr}}\left[\dfrac{\sigma_{xx}(\varepsilon_{xx})}{\sigma_n^0}\right]^2, & \min\left\{\dfrac{\sigma_n^0}{E_m}, \dfrac{(1+\Lambda_{cr})\Lambda}{(1+\Lambda)\Lambda_{cr}}\dfrac{\sigma_n^0}{E_m}\right\} \le \varepsilon_{xx} < \max\left\{\dfrac{\sigma_n^0}{E_m}, \dfrac{(1+\Lambda_{cr})\Lambda}{(1+\Lambda)\Lambda_{cr}}\dfrac{\sigma_n^0}{E_m}\right\} \\ \dfrac{1+\Lambda_{cr}}{\Lambda_{cr}}, & \varepsilon_{xx} \ge \dfrac{(1+\Lambda_{cr})\Lambda}{(1+\Lambda)\Lambda_{cr}}\dfrac{\sigma_n^0}{E_m} \end{cases} \tag{22}$$

where $U_I^0 = \int_0^{\delta_n^0} \sigma_n d\delta_n$ is the interface dissipation energy when $\delta_n = \delta_n^0$, and $\sigma_{xx}(\varepsilon_{xx})$ is the overall stress-strain relationship given by Eq. (19).

The elastic strain energy stored in the matrix is calculated by $U_E = \int_0^{(\varepsilon_{xx})_m} \sigma_{xx} d(\varepsilon_{xx})_m \cdot L$. Since the matrix is linear elastic, U_E is given by

$$\frac{U_E}{U_I^0} = \frac{\frac{1}{2}\frac{(\sigma_{xx})^2}{E_m}L}{\frac{1}{2}\frac{(\sigma_n^0)^2}{k_n}} = \frac{1}{\Lambda}\left[\frac{\sigma_{xx}(\varepsilon_{xx})}{\sigma_n^0}\right]^2 \tag{23}$$

It can be found that the elastic strain energy is also a piecewise linear function if we substitute Eq. (19) in Eq. (23).

The external work U_T, the interface dissipation energy U_I and the elastic strain energy U_E are plotted against the overall strain for several values of Λ in Fig. 5. It can be seen that all energies increase at first with the increase of the overall strain. As the normalized overall strain reaches $E_m\varepsilon_{xx}/\sigma_n^0 = 1.0$ for the first time, cohesive elements enter the softening stages. The interface dissipation energy U_I increases continuously while elastic strain energy U_E decreases. But whether the external work U_T increases or decreases is associated with the values of Λ and Λ_{cr}.

The changes of energies in the softening stage of cohesive elements can be expressed by

$$\begin{cases} \Delta U_I = U_I(\delta_n = \delta_n^f) - U_I(\delta_n = \delta_n^0) = \Gamma_n - \dfrac{(\sigma_n^0)^2}{2k_n} > 0 \\ \Delta U_E = U_E(\delta_n = \delta_n^f) - U_E(\delta_n = \delta_n^0) = -\dfrac{(\sigma_n^0)^2 L}{2E_m} < 0 \\ \Delta U_T = U_T(\delta_n = \delta_n^f) - U_T(\delta_n = \delta_n^0) = \Delta U_I + \Delta U_E \end{cases} \tag{24}$$

$\Delta U_I > 0$ and $\Delta U_E < 0$ imply that interface dissipation energy increases while elastic strain energy is released. Note that the ratio of Λ and Λ_{cr} can be written as

$$\frac{\Lambda}{\Lambda_{cr}} = \frac{E_m}{k_n L}\left(\frac{\delta_n^f}{\delta_n^0} - 1\right) = \frac{\Gamma_n - \frac{1}{2}\frac{(\sigma_n^0)^2}{k_n}}{\frac{1}{2}\frac{(\sigma_n^0)^2 L}{E_m}} = \frac{\Delta U_I}{|\Delta U_E|} \tag{25}$$

similar to the discussion of Hamitouche et al. (2008). Thus, in the softening stage, whether the change of external work ΔU_T is positive or negative depends on the relative size of Λ and Λ_{cr}.

When $\Lambda < \Lambda_{cr}$, as shown in Fig. 5(a), it can be seen that $|\Delta U_E| > \Delta U_I$ from Eq. (25), i.e., the released elastic strain energy $|\Delta U_E|$ exceeds the increase of interface dissipation energy ΔU_I. Considering energy conservation, we obtain $\Delta U_T = \Delta U_I + \Delta U_E < 0$. Thus, the system has to snap back, i.e., to reduce the overall strain, to make cohesive elements fracture. This can also be explained by noting that the system has to do work on the sur-

roundings to consume the excessive elastic strain energy since $-\Delta U_E = \Delta U_I + (-\Delta U_T) > 0$. In Fig. 5(a), the snap-back phenomenon is observed when the normalized overall strain decreases from 1.0 to about 0.5. At last, the fracture of cohesive elements occurs, i.e., $U_I = \Gamma_n$, and the elastic strain energy is released completely.

The case of $\Lambda = \Lambda_{cr}$ shown in Fig. 5(b) is a critical state. In the softening stage, the increment of interface dissipation energy ΔU_I is equal to the released elastic strain energy $|\Delta U_E|$. Consequently, $\Delta U_T = \Delta U_I + \Delta U_E = 0$, i.e., the external work remains unchanged. And the fracture occurs instantaneously as soon as the normalized overall strain reaches 1.0. For $\Lambda > \Lambda_{cr}$, as illustrated in Fig. 5(c), the increment of interface dissipation energy ΔU_I exceeds the released elastic strain energy $|\Delta U_E|$. Consequently, $\Delta U_T = \Delta U_I + \Delta U_E > 0$, i.e., the overall strain increases continuously to make the cohesive elements fracture and no snap-back behavior occurs.

The snap-back instability always causes convergence problems in implicit finite element simulations using Newton–Raphson method, since no solutions will be found with continuously increasing overall strain. From Eq. (25), with the increase of fracture toughness Γ_n, stiffness k_n and Young's modulus E_m, or the decrease of strength σ_n^0 and length L, the value of Λ/Λ_{cr} increases, i.e., the snap-back behaviors are less likely to happen. It should be noted that when stiffness k_n tends to infinity (or thickness $t_0 = E_m/k_n$ tends to zero), there is an upper bound of Λ/Λ_{cr}: $2E_m\Gamma_n/[(\sigma_n^0)^2 L]$. In the case of the upper bound less than 1, convergence problems due to the snap-back instability are inevitable whatever the value of stiffness k_n is. In order to overcome possible convergence problems, a lot of strategies have been proposed, including arc-length algorithm (Riks, 1979) to follow the snap-back branch, and viscous regularization (Chaboche et al., 2001; Gao and Bower, 2004; Hamitouche et al., 2008) to consume excessive elastic strain energy by introducing viscosity.

4. Bi-material systems with cohesive elements at interface

4.1. Thickness-dependent failure characteristics

Cohesive elements can also be used to model the interface layer of bi-material systems, for example, the thin adhesive layer of adhesive joints. For the equivalence of cohesive elements and an undamaged adhesive layer (Távara et al., 2011), selection criterion of stiffness like Eq. (14) is applicable. In this case, E_m and ν_m denote the Young's modulus and Poisson's ratio of the adhesive, respectively, and t_0 is the adhesive thickness. Considering that the adhesive layer confined between two stiff adherends cannot expand or contract freely in the lateral direction (Sarrado et al., 2016; Távara et al., 2011), the selection criterion of stiffness can be modified further. However, if we do not focus on what the interface layer is specifically, the selection criterion of stiffness of finite-thickness cohesive elements is not needed, and zero-thickness cohesive elements are sufficient to characterize the interface of bi-material systems. In this case, the stress-displacement relationship independent of the thickness of cohesive elements, rather than the stress-strain relationship, is used to describe the overall mechanical responses.

By analyzing the overall mechanical responses of bi-material systems with cohesive elements at interface, a thickness-dependent failure characteristic, similar to that revealed by You et al. (2018) in atomistic simulations, will be revealed combined with a theoretic explanation. Fig. 6 shows zero-thickness cohesive elements are inserted at interface of the cylindrical bi-material system composed of two kinds of materials. The moduli and thicknesses of these materials are denoted by E_i $(i = 1, 2)$ and h_i $(i = 1, 2)$, respectively. The Poisson's ratios are assumed to be

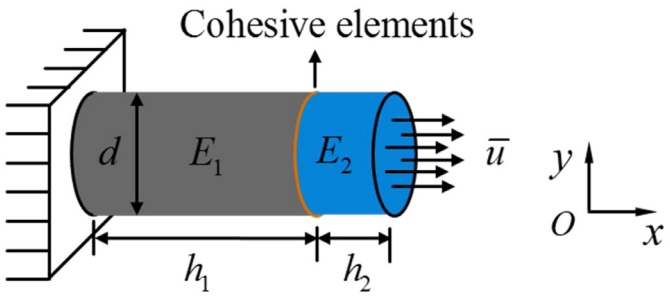

Fig. 6. Schematic illustration of a bi-material system with a layer of cohesive elements in uniaxial tension.

zero, and thus the following results are independent of the diameter d.

When the system is in uniaxial tension, the overall elongation of the system, i.e., the horizontal loading displacement of the right boundary $\bar{u}$, can be divided into three parts: elongation of cohesive elements and those of the surrounding materials, and thus it can be expressed by

$$\bar{u} = \frac{\sigma_{xx}}{E_1} h_1 + \frac{\sigma_{xx}}{E_2} h_2 + \delta_n \tag{26}$$

Substituting Eq. (1) in Eq. (26) and considering $\sigma_{xx} = \sigma_n$, the overall stress-displacement relationship can be obtained:

$$\frac{\sigma_{xx}}{\sigma_n^0} = \begin{cases} \frac{\Lambda'}{1+\Lambda'}\frac{\bar{u}}{\delta_n^0}, \frac{\bar{u}}{\delta_n^0} < \frac{1+\Lambda'}{\Lambda'} \\ \frac{\Lambda'\Lambda_{cr}}{\Lambda_{cr}-\Lambda'}\frac{\bar{u}}{\delta_n^0} - \frac{(1+\Lambda_{cr})\Lambda'}{\Lambda_{cr}-\Lambda'}, \min\left\{\frac{1+\Lambda'}{\Lambda'}, \frac{1+\Lambda_{cr}}{\Lambda_{cr}}\right\} \le \frac{\bar{u}}{\delta_n^0} < \max\left\{\frac{1+\Lambda'}{\Lambda'}, \frac{1+\Lambda_{cr}}{\Lambda_{cr}}\right\} \\ 0, \frac{\bar{u}}{\delta_n^0} \ge \frac{1+\Lambda_{cr}}{\Lambda_{cr}} \end{cases} \tag{27}$$

where Λ' and Λ_{cr} are two dimensionless quantities defined by

$$\Lambda' = \frac{E_1 E_2}{k_n(E_1 h_2 + E_2 h_1)}, \Lambda_{cr} = \frac{\delta_n^0}{\delta_n^f - \delta_n^0} \tag{28}$$

Taking Eq. (1) into Eq. (27) to eliminate σ_{xx}, the relationship between interface separation and the overall displacement can be obtained:

$$\frac{\delta_n}{\delta_n^0} = \begin{cases} \frac{\Lambda'}{1+\Lambda'}\frac{\bar{u}}{\delta_n^0}, \frac{\bar{u}}{\delta_n^0} < \frac{1+\Lambda'}{\Lambda'} \\ \frac{1+\Lambda_{cr}}{\Lambda_{cr}-\Lambda'} - \frac{\Lambda'}{\Lambda_{cr}-\Lambda'}\frac{\bar{u}}{\delta_n^0}, \min\left\{\frac{1+\Lambda'}{\Lambda'}, \frac{1+\Lambda_{cr}}{\Lambda_{cr}}\right\} \le \frac{\bar{u}}{\delta_n^0} < \max\left\{\frac{1+\Lambda'}{\Lambda'}, \frac{1+\Lambda_{cr}}{\Lambda_{cr}}\right\} \\ \frac{\bar{u}}{\delta_n^0}, \frac{\bar{u}}{\delta_n^0} \ge \frac{1+\Lambda_{cr}}{\Lambda_{cr}} \end{cases} \tag{29}$$

Similar discussions like snap-back instability can be performed. We only consider the stable case here, i.e., $\Lambda' \ge \Lambda_{cr}$. In the softening stage of the overall stress-displacement relationship, which corresponds to the softening stage of cohesive elements, the decreasing rate of stress and the increasing rate of separation can be obtained respectively from Eqs. (27) and (29):

$$\begin{cases} \left|\frac{d\sigma_{xx}}{d\bar{u}}\right| = \frac{k_n\Lambda_{cr}}{1-\Lambda_{cr}/\Lambda'} \\ \frac{d\delta_n}{d\bar{u}} = \frac{1}{1-\Lambda_{cr}/\Lambda'} \end{cases} \frac{1+\Lambda'}{\Lambda'} \le \frac{\bar{u}}{\delta_n^0} \le \frac{1+\Lambda_{cr}}{\Lambda_{cr}} (\Lambda' \ge \Lambda_{cr}) \tag{30}$$

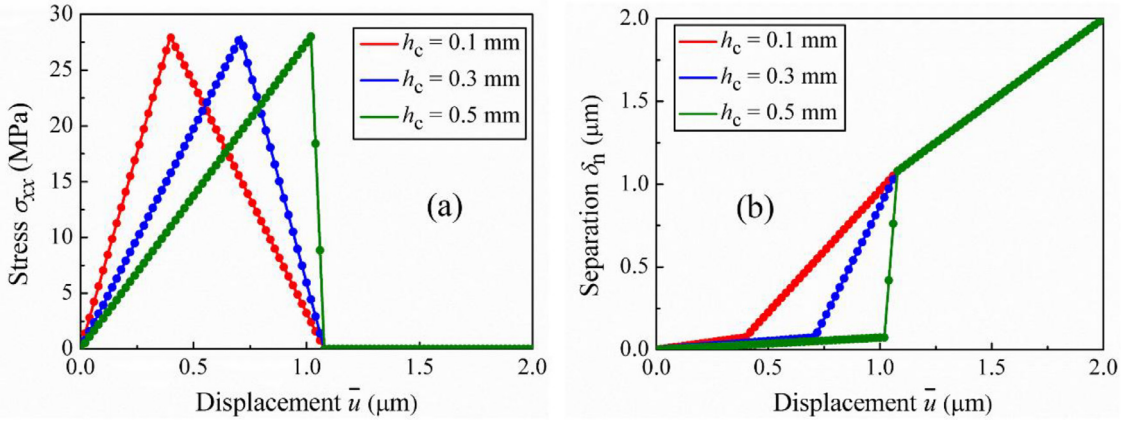

Fig. 7. (a) The overall stress–displacement relationship, and (b) the interface separation-overall displacement relationship of the coating/substrate systems with different coating thicknesses. The solid lines are theoretical results based on Eqs. (27) and (29) respectively in (a) and (b) and the symbols are simulation results based on FEM.

With the increase of h_1 and h_2, Λ'decreases monotonously from Eq. (28). The decreasing rate of stress and the increasing rate of separation thus increase based on Eq. (30). When Λ'decreases to Λ_{cr}, the increasing rate of separation is infinity and the failure is completely catastrophic. Thus, for larger bi-material systems, the fracture is faster and the failure tends to be more catastrophic, i.e., closer to completely catastrophic failure.

Replacing $\sigma_{xx}(\varepsilon_{xx})$ and Λ with $\sigma_{xx}(\bar{u})$ and Λ' respectively in Eqs. (22) and (23), all kinds of energies for bi-material systems with cohesive elements can be obtained. Energy analysis can also be used to explain the influences of thickness, which will be shown in the following simulations based on FEM.

4.2. Numerical verification

In this section, we take the ceramic coating/superalloy substrate system with cohesive elements as an example to investigate the influences of the coating thickness by means of FEM. The simulation results will be compared with theoretical predictions.

The ceramic coating is considered as linear elastic material with Young's modulus of $E_c = 18$ GPa (Rabiei and Evans, 2000). The coating thickness h_c varies from 0.1 mm to 0.5 mm. The superalloy substrate is assumed as linear elastic for simplicity and its modulus is $E_s = 200$ GPa (Zhu et al., 2015a), and its thickness is $h_s = 1.2$ mm to compared with experiments (Liang et al., 2013). A layer of zero-thickness cohesive elements is inserted into the interface between the substrate and the coating. The parameters of the cohesive elements are $k_n = 3.78 \times 10^5$MPa/mm, $\sigma_n^0 = 28$MPa and $\Gamma_n^0 = 15.1$J/m^2 (Liang et al., 2013). From Eq. (28), when $h_c = 0.5$ mm, Λ' takes the minimum value, $\Lambda'_{min} = 0.078 > \Lambda_{cr} = 0.074$ with $\delta_n^0 = 0.07\mu$m and $\delta_n^f = 1.1\mu$m (Liang et al., 2013), which indicates that no snap-back instability occurs here.

Fig. 7(a) shows the relation curves between stress and the loading displacement. It can be found that the simulation results based on FEM match well with theoretical predictions based on Eq. (27). With the increase of coating thickness, the stress drops faster after it reaches its maximum value. Correspondingly, as illustrated in Fig. 7(b), the interface separation increases faster from the critical displacement δ_n^0 to the fracture displacement δ_n^f. Thus, as the coating thickness increases, the fracture tends to be more catastrophic.

We can find explanations from energy analysis as well. The external work U_T, the interface dissipation energy consumed by cohesive elements U_I, and the elastic strain energy stored in the coating and the substrate U_E with the loading displacement are shown in Fig. 8. Similar to Eq. (24), $\Delta U_T > 0$, $\Delta U_I > 0$ and $\Delta U_E < 0$ denote the change of external work energy, interface dissipation energy, and elastic strain energy in the softening stage of cohesive elements, respectively. Noting that $\Delta U_I = \Delta U_T - \Delta U_E$ according to energy conservation, it can be seen that the sum of the increased external work and released elastic strain energy is consumed by interface dissipation. As shown in Fig. 8, with the increase of coating thickness from 0.1(Fig. 8(a)), 0.3 (Fig. 8(b)) to 0.5 mm (Fig. 8(c)), ΔU_I is fixed, but the released elastic strain energy $|\Delta U_E|$ increases. Thus, less external work ΔU_T, i.e., less increase of loading displacement $\bar{u}$, is needed to make the system fracture, which can be seen from $\Delta\bar{u}_1 > \Delta\bar{u}_2 > \Delta\bar{u}_3$ in Fig. 8. Consequently, with the increase of coating thickness, the elastic strain energy releases more rapidly and the fracture of cohesive elements is more abruptly, i.e., the failure tends to be more catastrophic. These results are similar to the phenomena revealed by atomistic simulations of Ag/MgO interface tension (You et al., 2018), although the length scale considered here is much larger.

5. Failure of ceramic coating/substrate systems with cohesive elements in coating and interface

In the previous sections, the overall responses of single-material media and bi-material systems with cohesive elements in uniaxial tension are investigated respectively. In this section, more complex systems, i.e., the ceramic coating/substrate systems under three-point bending are considered. Cohesive elements are simultaneously inserted into the coating and the interface, and then the failure behaviors involved with coating cracking and interface delamination are simulated by means of FEM.

5.1. Finite element model with cohesive elements

Ceramic coating/substrate systems are assumed to be under the plane strain condition and the two dimensional finite element analysis was carried out using the commercial software ABAQUS. As illustrated in Fig. 9, only the left half is considered due to the symmetry of the model. The frictionless indenter and supports with radii of $R_1 = 0.9$ mm are considered as rigid bodies. Vertical loading displacement w is applied on the indenter while the supports remain fixed. The span length and the total length of the system are $L = 16$ mm and $L_T = 20$ mm, respectively. The model includes two layers: substrate with thickness of $h_s = 1.2$ mm and ceramic coating with thickness of h_c. Subscripts s and c represent substrate and coating, respectively. The dimensionless coating thickness h_c/h_s varies from 0.1 to 0.4 to investigate its influence.

Ceramic coating is considered as linear elastic material with Young's modulus of $E_c = 18$ GPa and Poisson's ratio of $\nu_c = 0.2$ (Rabiei and Evans, 2000). Superalloy substrate is assumed to be

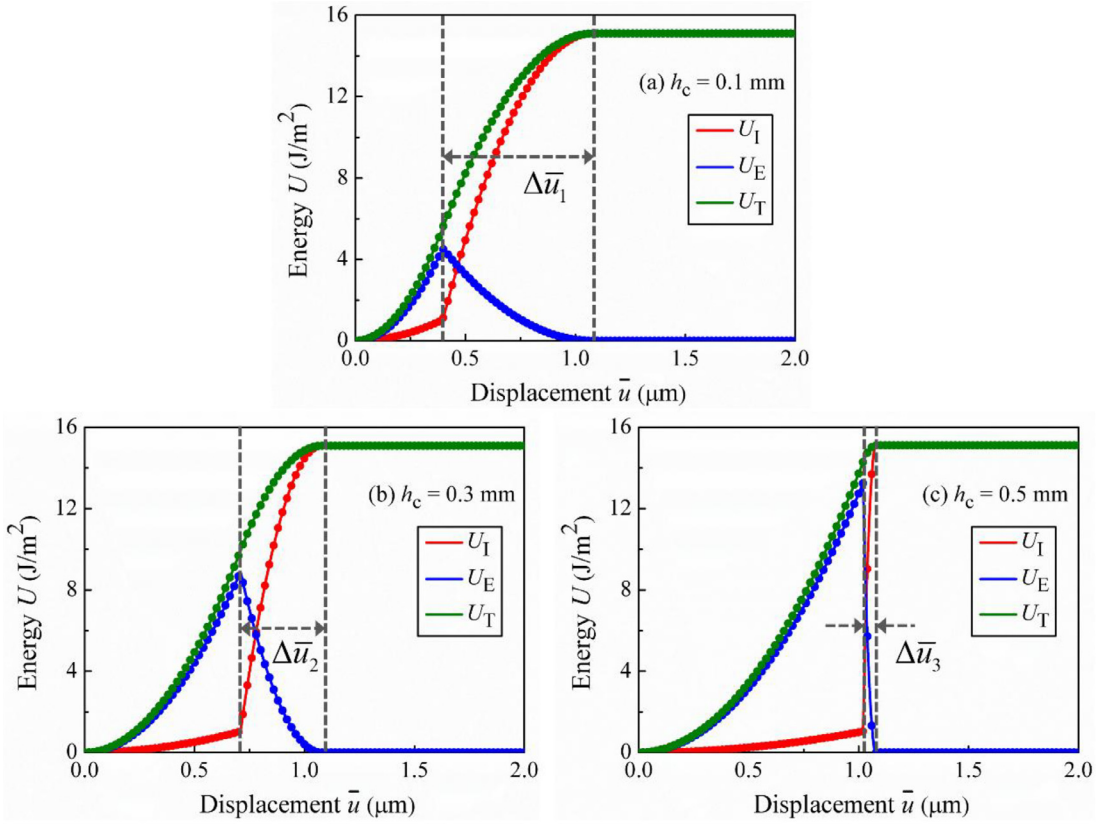

Fig. 8. The external work U_T, the interface dissipation energy U_I, and the elastic strain energy U_E versus the loading displacement for coating/substrate systems with different coating thicknesses: (a) $h_c = 0.1$ mm; (b) $h_c = 0.3$ mm; (c) $h_c = 0.5$ mm. The solid lines are theory results and the symbols are simulation results based on FEM.

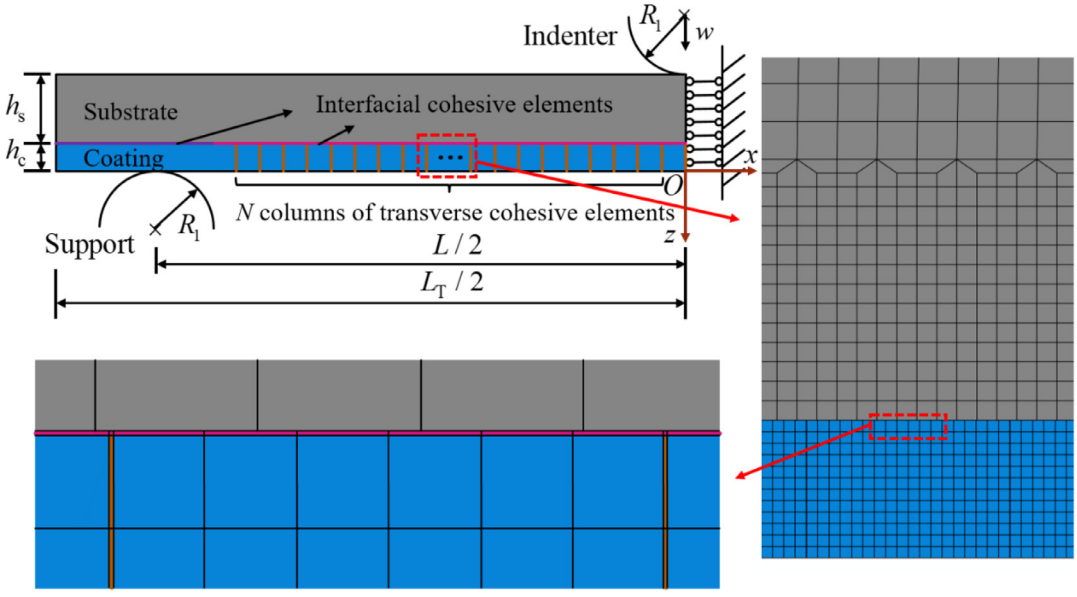

Fig. 9. Finite element model of a ceramic system under three-point bending loading, with a layer of cohesive elements in the interface of coating/substrate and multi-layer cohesive elements in the coating of thickness $h_c/h_s = 0.1$. Refined mesh near the interface is presented.

elastic-plastic material with Young's modulus of $E_s = 200$ GPa and Poisson's ratio of $\nu_s = 0.3$ (Zhu et al., 2015a), and its constitutive relation is given by

$$\varepsilon = \begin{cases} \sigma/E_s, \sigma \le \sigma_Y \\ (\sigma_Y/E_s)(\sigma/\sigma_Y)^{1/n}, \sigma > \sigma_Y \end{cases} \tag{31}$$

where ε is strain, σ is stress, $\sigma_Y = 800$ MPa is the yield stress and $n = 0.1$ is the power hardening exponent.

To model coating cracking and interface delamination, transverse and interface cohesive elements are inserted into coating and interface at the same time as shown in Fig. 9. From now on, we use the superscripts (T) and (I) to refer to transverse and interface cohesive elements, respectively. The thickness of transverse cohe-

sive elements $t_0^{(T)}$ is related to their stiffness $k_i^{(T)}(i = n, t)$ according to the selection criterion proposed in Section 3.1. The number of columns of transverse cohesive elements is $2N+1=201$, which is determined until the crack distribution tends to be stable with increasing the value of N. The thickness of interfacial cohesive elements $t_0^{(I)}$ is equal to that of transverse cohesive elements $t_0^{(T)}$ for convenience. And the interfacial strength in the purple region are set large enough to suppress delamination near the supports. The quadratic nominal stress criterion and the power law criterion for mixed-mode I and II loading are adopted here.

For simplicity, values of strength and fracture toughness of cohesive elements in normal and tangential directions are assumed to be the same (Li et al., 2014; Zhu et al., 2014), i.e., $\sigma_n^{0(T)} = \sigma_t^{0(T)}$, $\Gamma_n^{(T)} = \Gamma_t^{(T)}$, $\sigma_n^{0(I)} = \sigma_t^{0(I)}$ and $\Gamma_n^{(I)} = \Gamma_t^{(I)}$. And the relation of interfacial stiffness $k_n^{(I)} = k_t^{(I)}$ is assumed as well. For given geometry and material parameters except coating thickness and parameters of cohesive elements, dimensionless analysis indicates that the dimensionless transverse crack length $l^{(T)}$ (or interface crack length with superscript (I)) can be expressed as

$$\frac{l^{(T)}}{h_s} = f\left(\frac{w}{h_s}, \frac{h_c}{h_s}, \frac{k_n^{(T)}h_s}{\sigma_Y}, \frac{\sigma_n^{0(T)}}{\sigma_Y}, \frac{\Gamma_n^{(T)}}{\sigma_Y h_s}, \frac{k_n^{(I)}h_s}{\sigma_Y}, \frac{\sigma_n^{0(I)}}{\sigma_Y}, \frac{\Gamma_n^{(I)}}{\sigma_Y h_s}\right) \tag{32}$$

As mentioned, dimensionless coating thickness h_c/h_s varies from 0.1 to 0.4. The thickness of transverse cohesive elements is selected as $t_0^{(T)}/h_s = 1\times10^{-4}$, which indicates a small volume change noting that $(2N+1)t_0^{(T)}/L = 0.15\%$. Invoking the selection criterion of Eq. (15), stiffness of transverse cohesive elements is selected as follows:

$$\begin{cases} \dfrac{k_n^{(T)}h_s}{\sigma_Y} = \dfrac{E_c/\sigma_Y}{(1-\nu_c^2)t_0^{(T)}/h_s} = 2.34\times10^5 \\ \dfrac{k_t^{(T)}h_s}{\sigma_Y} = \dfrac{1-\nu_c}{2}\dfrac{k_n^{(T)}h_s}{\sigma_Y} = 9.38\times10^4 \end{cases} \tag{33}$$

Thus, we can ensure that the introduction of transverse cohesive elements does not affect the elastic constants of the ceramic coating. As for interfacial cohesive elements, large values of stiffness are selected, i.e., $k_n^{(I)}h_s/\sigma_Y = 1\times10^4$.

To check the effect of cohesive parameters, dimensionless strength and fracture toughness of transverse and interfacial cohesive elements can be selected in the following range: $\sigma_n^{0(T)}/\sigma_Y = 0.03\sim0.16$, $\Gamma_n^{(T)}/(\sigma_Y h_s) = (1.0\sim5.1)\times10^{-5}$, $\sigma_n^{0(I)}/\sigma_Y = 0.01\sim0.10$, and $\Gamma_n^{(I)}/(\sigma_Y h_s) = (1\sim16)\times10^{-5}$ considering $\sigma_Y = 800$ MPa and $h_s = 1.2$ mm. The strength and fracture toughness of cohesive elements are consistent with previous reports in literatures. The tensile strength of ceramic coating varies from 25 to 125 MPa (Wan et al., 2013; Zhu et al., 2014), and the fracture toughness of ceramic coating is about 10~49 J/m^2 (Rabiei and Evans, 2000). The interfacial strength of ceramic coating/superalloy substrate systems varies from 8 to 80 MPa (Di Leo et al., 2014; Zhu et al., 2014), and the interfacial fracture toughness is between 10 and 150 J/m^2 (Liang et al., 2013; Zhu et al., 2014).

As discussed in Section 3.2, convergence problems due to the snap-back instability are always encountered in finite element simulations using CZMs. Here, viscous regularization (Dassault Systèmes, 2014; Simonovski and Cizelj, 2013) is adopted to overcome convergence problems by adding the viscosity that introduces artificial energy dissipation. A small value of viscosity parameter $\mu = 0.0001$ is selected to guarantee the convergence but minimize its influences on the physical solution, which is similar to the choices in previous studies (Li et al., 2014; Zhu et al., 2015b).

The four-node plane strain reduced integration elements (CPE4R) are selected to mesh substrate and coating. The four-node cohesive elements (COH2D4) are inserted into the coating and the interface. In the regions near supports, indenter and interface, finite element mesh is refined. Refined mesh near the interface is shown in Fig. 9.

5.2. Thickness-dependent damage and failure

In order to investigate the influence of coating thickness, parameters of cohesive elements are selected from the range given above and fixed at $\sigma_n^{0(T)}/\sigma_Y = 0.05$, $\Gamma_n^{(T)}/(\sigma_Y h_s) = 2\times10^{-5}$, $\sigma_n^{0(I)}/\sigma_Y = 0.04$, and $\Gamma_n^{(I)}/(\sigma_Y h_s) = 3\times10^{-5}$.

Considering that the cohesive element size should be small enough to represent the stress distribution accurately inside the cohesive zone (Tomar et al., 2004; Turon et al., 2007), a proper length of cohesive elements (the thickness of cohesive elements is fixed at a small value) should be chosen to make the simulation results mesh-independent. Since the sizes of transverse and interfacial cohesive elements are very close, only the former $l_{CE}^{(T)}$ is considered. Taking the system with coating thickness of $h_c/h_s = 0.3$ as an example, the mesh sensitivity analysis was carried out by reducing the cohesive element length and refining the mesh in the vicinity of the support, the indenter as well as the interface. The simulation results with three different meshes are shown in Fig. 10. The ratio of cohesive element length to cohesive element thickness for the coarsest mesh is $l_{CE}^{(T)}/t_0^{(T)} = 83$. The number of cohesive elements along the coating thickness direction is 36 for the coarsest mesh ($l_{CE}^{(T)}/h_c = 0.028$) and this number doubles for the finest mesh ($l_{CE}^{(T)}/h_c = 0.014$). According to Fig. 10, when the ratio of cohesive element length to coating thickness decreases from $l_{CE}^{(T)}/h_c = 0.028$ to $l_{CE}^{(T)}/h_c = 0.014$ (correspondingly, the total number of elements of this model increases from 5.3×10^4 to 1.7×10^5), the relative change of transverse crack length or interfacial crack length for a fixed loading displacement is less than 2%, which indicates that the crack evolution tends to be convergent. Thus the coarsest mesh is acceptable for our simulations, and the corresponding mesh size is what we adopted eventually.

The fracture maps of systems with different coating thicknesses are shown in Fig. 11. As coating thickness increases from (a) to (d), the number of transverse cracks decreases, while the delamination length increases continuously. This is corresponding to the transition of dominant failure mode from coating cracking to interface delamination. Fig. 12 shows similar phenomena observed in our experiments as reported previously (Li et al., 2014), which validates simulations results based on FEM.

Curves of transverse crack length and interfacial crack length as a function of loading displacement for systems with different coating thicknesses are shown in Fig. 13. Each curve can be divided into three stages: initiation, multiplication and saturation of cracks. Interestingly, crack evolution is different for systems with different coating thicknesses. Fig. 13(a) and (b) show that the thicker the coating is, the earlier the transverse crack and the interfacial crack initiates. Furthermore, in the initial stage of loading ($w/h_s \le 0.2$), for systems with thin coatings ($h_c/h_s = 0.1$, 0.2 and 0.3), transverse crack length is larger than interfacial crack length. But for systems with thick coating ($h_c/h_s = 0.4$), interfacial crack length is larger than transverse crack length. Therefore, the dominated failure mode is coating cracking for thin coating systems while it is interface delamination for thick coating systems.

The influence of coating thickness on failure behaviors can be traced back to the stress distribution before crack occurs. From composite beam theory and plane strain condition, the bending stress in the coating on the midspan section is given by

$$\sigma_{xx} = \frac{PL}{4}\frac{E_{c1}(z-z_0)}{\bar{E}\bar{I}},\quad -h_c \le z \le 0 \tag{34}$$

where $\bar{E}\bar{I} = E_{s1}\int_{-(h_s+h_c)}^{-h_c}(z-z_0)^2dz + E_{c1}\int_{-h_c}^{0}(z-z_0)^2dz$ is the equivalent bending stiffness, $z_0 = -(E_{s1}h_s^2 + E_{c1}h_c^2 + 2E_{s1}h_sh_c)/$

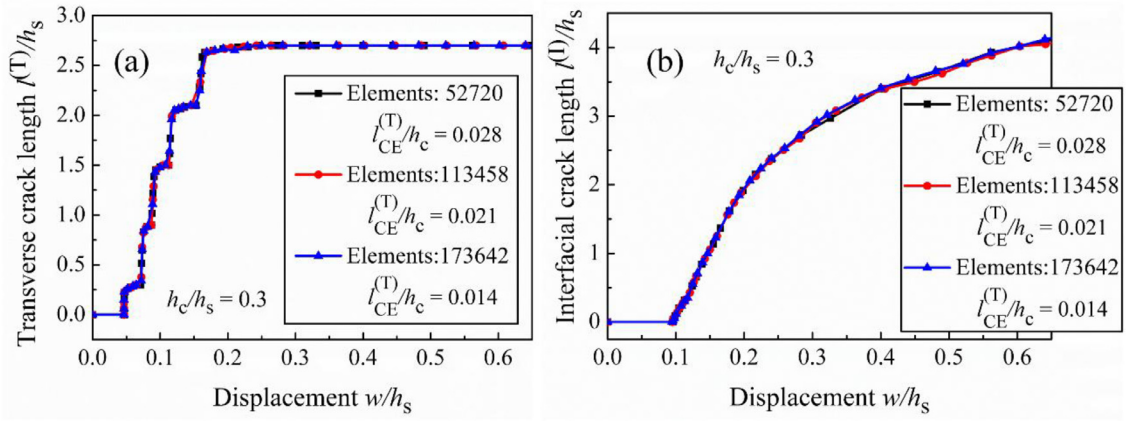

Fig. 10. The simulation results with three different meshes for the model with coating thickness of $h_c/h_s = 0.3$: (a) transverse crack length versus loading displacement, and (b) interfacial crack length versus loading displacement.

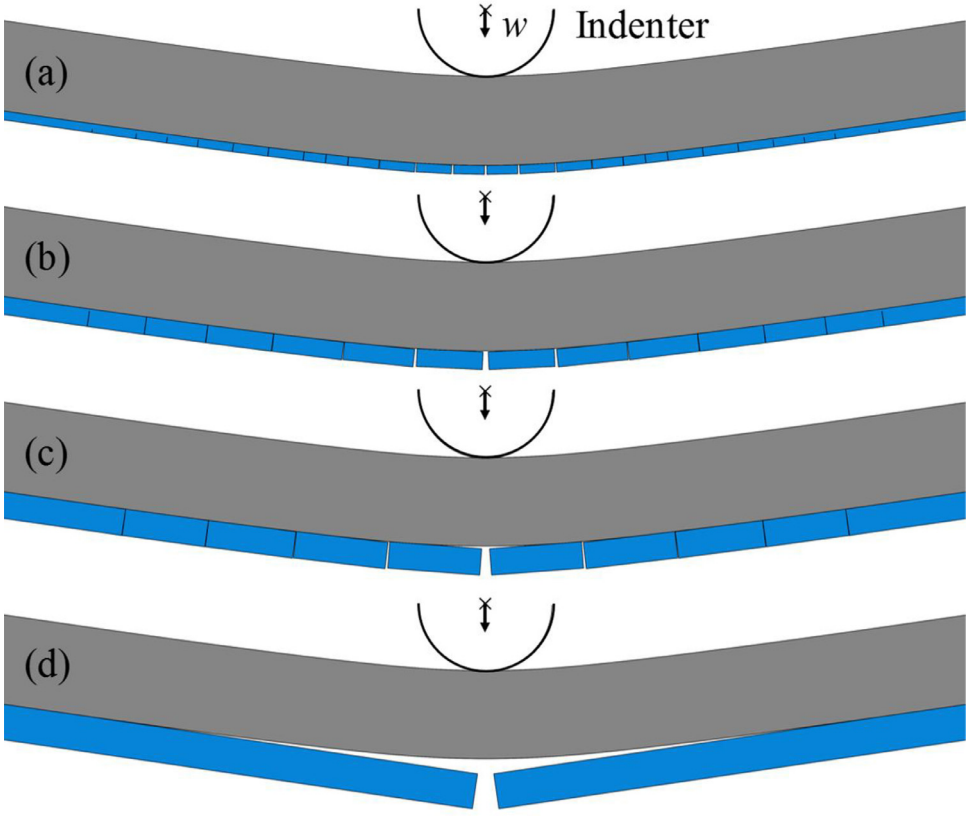

Fig. 11. The fracture maps of systems with coating thickness of (a) $h_c/h_s = 0.1$, (b) $h_c/h_s = 0.2$, (c) $h_c/h_s = 0.3$, and (d) $h_c/h_s = 0.4$ when the loading displacement is $w/h_s = 0.8$.

$[2(E_{s1}h_s + E_{c1}h_c)]$ denotes the location of neutral plane, $E_{c1} = E_c/(1-\nu_c{}^2)$, and $E_{s1} = E_s/(1-\nu_s{}^2)$. Interfacial normal stress σ_{zz} is always zero, while interfacial shear stress is given by

$$\tau_{zx} = \frac{P}{4}\frac{E_{s1}(h_s{}^2 + 2h_s h_c + 2h_s z_0)}{\bar{E}\bar{I}} \tag{35}$$

The bending stress in the coating and interfacial shear stress are shown in Fig. 14(a) and (b), respectively. It can be seen that theoretical results based on Eqs. (34) and (35) and simulation results based on FEM match well. For a given coating thickness, the bending stress varies linearly along the thickness direction and reaches a maximum at the coating surface ($z = 0$), as shown in Fig. 14(a). The thicker the coating is, the larger the tensile stress at the coating surface is, which explains the earlier initiation of transverse cracks for thick coating systems. While the interfacial shear stress is almost a constant along the interface, as shown in Fig. 14(b), except the simulated results at the left end and at the midspan ($x = 0$). Some minute oscillations of interfacial shear stress due to the intersection of transverse and interfacial cohesive elements can be neglected. By a comparison of interface shear stresses at various coating thicknesses, it can be found that the interfacial shear stress increases with increasing coating thickness, and the increasing interfacial shear stress with coating thickness leads to the transition of dominant failure mode from coating cracking to interface delamination. The simulation results also show enhanced midspan and end effects with increasing coating thickness.

According to a power-law damage and catastrophic failure model (Hao et al., 2013; Liang et al., 2016), the damage, defined by crack length, can be characterized from the damage initiation

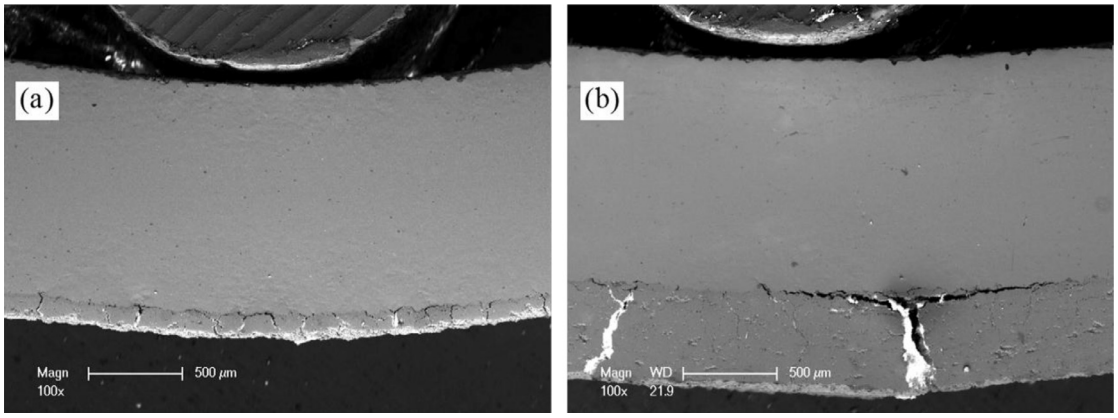

Fig. 12. The fracture maps of systems with coating thickness of (a) $h_c = 100\,\mu$m and (b) $h_c = 500\,\mu$m observed in the experiments, the experimental detail can be referred to the previous work (Li et al., 2014).

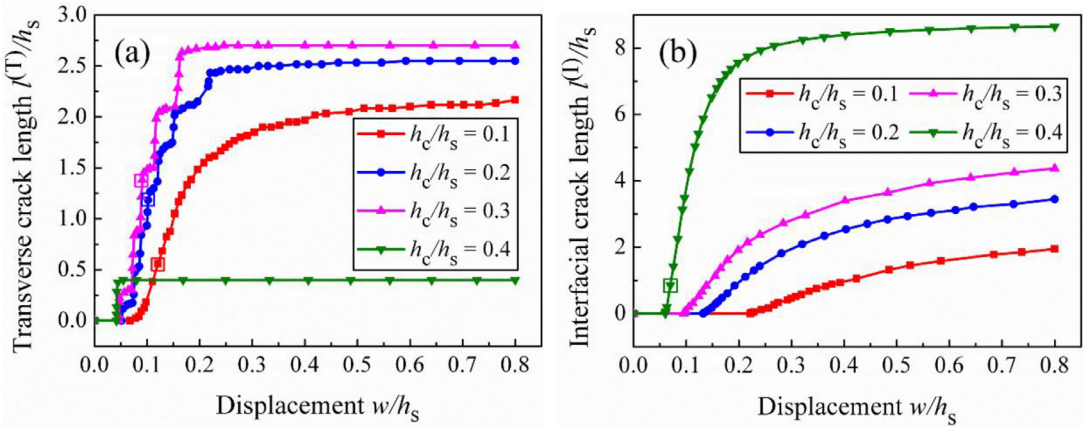

Fig. 13. Crack evolution of systems with different coating thicknesses: (a) transverse crack length versus loading displacement, and (b) interfacial crack length versus loading displacement. The rectangle frames denote the catastrophic failure points.

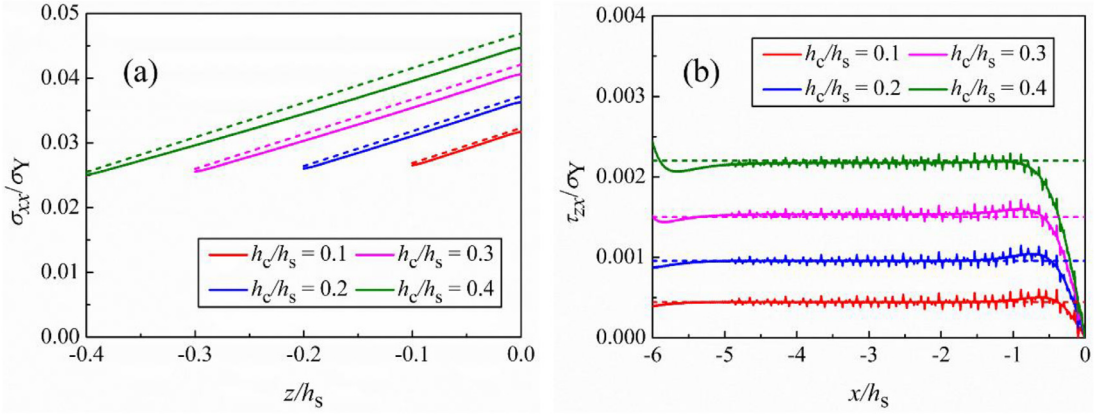

Fig. 14. Stress distribution of systems with different coating thicknesses when loading displacement is $w/h_s = 0.035$: (a) bending stress in the coating along the thickness direction on the midspan section with coating surface at $z = 0$; (b) interfacial shear stress along the interface. The solid lines are simulation results based on FEM and the dashed lines are theoretical results based on Eqs. (34) and (35), respectively.

point to the failure point. Details of the model are introduced in Appendix B. For coating/substrate systems here, the damage initiation point is the moment when the first crack initiates. And the failure point marked by a rectangle frame in Fig. 13 is the moment at which the increasing rate of crack length reaches its maximum, which corresponds to that multiple transverse cracks emerge for thin coating systems as discussed in experimental observation (Liang et al., 2016). At the time near the failure point, the plastic deformation of the substrate is small, which implies the energy dissipation due to plastic deformation can be ignored. Only in this case, the failure of the system will show a brittle characteristic.

According the power-law model expressed by Eq. (B.2), the damage variable D as a function of the controlling variable λ obeys the power-law relation with the exponent of 0.5. For systems with thin coatings ($h_c/h_s = 0.1$, 0.2 and 0.3), the damage variable is defined by normalized transverse crack length: $D = l^{(T)}/l_f^{(T)}$, where subscript f denotes the failure point. While for system with thick coating ($h_c/h_s = 0.4$), the damage variable is defined by normalized

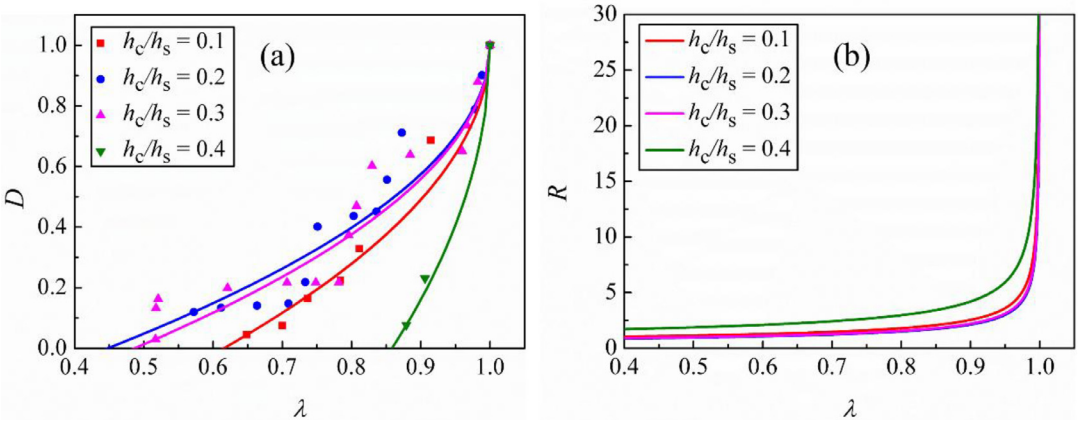

Fig. 15. Damage evolution of systems with different coating thicknesses: (a) the damage variable D versus the controlling variable λ, the symbols are the simulation results and the lines are results from Eq. (B.2), and (b) the damage rate R versus the controlling variable λ based on Eq. (B.3) with a coefficient C referring to the simulation results.

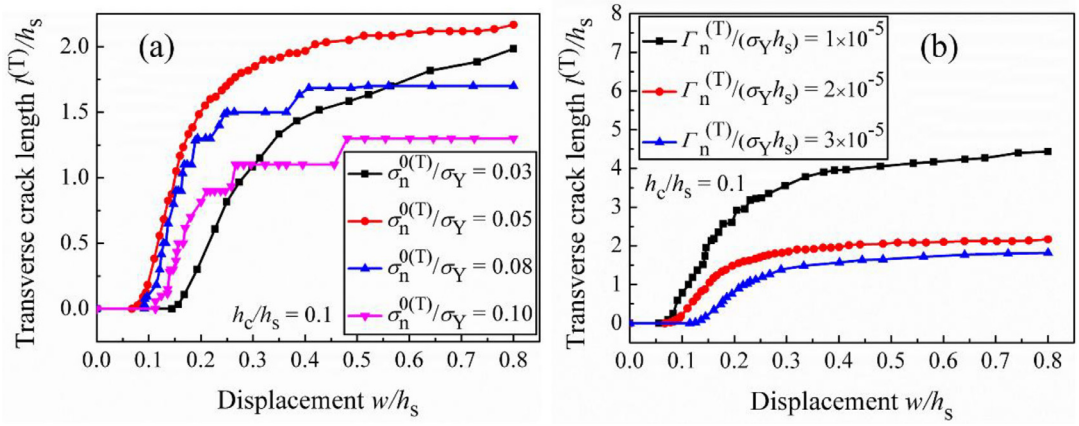

Fig. 16. Influences of parameters of transverse cohesive elements on transverse crack length as a function of loading displacement for systems with coating thickness of $h_c/h_s = 0.1$: (a) influence of coating strength for fixed $\Gamma_n^{(T)}/(\sigma_Y h_s) = 2 \times 10^{-5}$, $\sigma_n^{0(I)}/\sigma_Y = 0.04$, and $\Gamma_n^{(I)}/(\sigma_Y h_s) = 3 \times 10^{-5}$; (b) influence of coating fracture toughness for fixed $\sigma_n^{0(T)}/\sigma_Y = 0.05$, $\sigma_n^{0(I)}/\sigma_Y = 0.04$, and $\Gamma_n^{(I)}/(\sigma_Y h_s) = 3 \times 10^{-5}$.

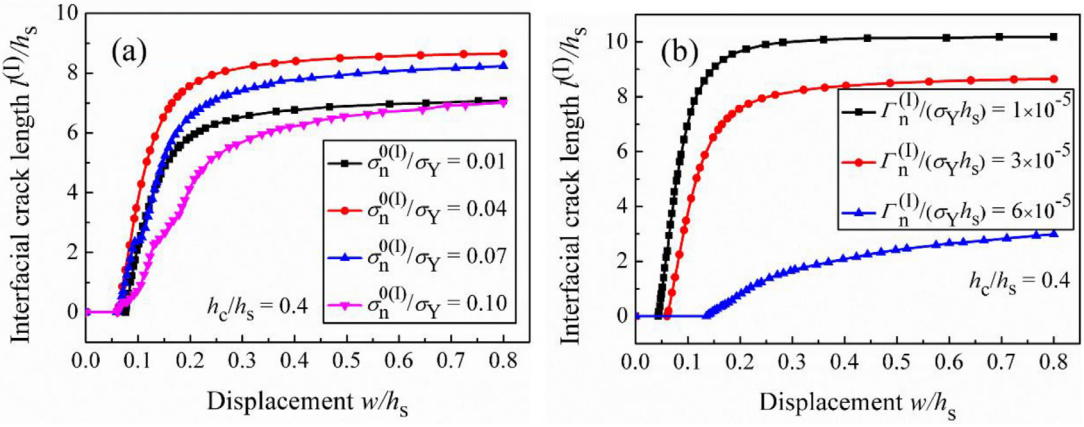

Fig. 17. Influences of parameters of interfacial cohesive elements on interfacial crack length as a function of loading displacement for systems with coating thickness of $h_c/h_s = 0.4$: (a) influence of interfacial strength for fixed $\sigma_n^{0(T)}/\sigma_Y = 0.05$, $\Gamma_n^{(T)}/(\sigma_Y h_s) = 2 \times 10^{-5}$, and $\Gamma_n^{(I)}/(\sigma_Y h_s) = 3 \times 10^{-5}$; (b) influence of interfacial fracture toughness for fixed $\sigma_n^{0(T)}/\sigma_Y = 0.05$, $\Gamma_n^{(T)}/(\sigma_Y h_s) = 2 \times 10^{-5}$, and $\sigma_n^{0(I)}/\sigma_Y = 0.04$.

interfacial crack length: $D = l^{(I)}/l_f^{(I)}$. The controlling variable is defined by the normalized loading displacement: $\lambda = w/w_f$.

For systems with different coating thicknesses, curves of damage evolution based on the power-law model are shown in Fig. 15(a). It can be seen that the symbols from the simulations are roughly in agreement with the curves predicted by the damage model. From Fig. 15(b), the damage rate R of the system with thick coating ($h_c/h_s = 0.4$) is larger than that of systems with thin coatings ($h_c/h_s = 0.1$, 0.2 and 0.3). Thus, the damage of thick coating systems with dominated failure mode of interface delamination is faster than that of thin coating systems with dominated failure mode of coating cracking, agreeing with experimental results (Liang et al., 2016).

Since the failure of thin coating systems is dominated by coating cracking, the influences of parameters of transverse cohesive elements on transverse crack length are investigated for systems with a thin coating of $h_c/h_s = 0.1$, as illustrated in Fig. 16. When coating strength increases from 0.03 to 0.05, as illustrated in Fig. 16(a), the transverse crack length increases, which is associated with the decrease of fracture displacement $\delta_n^{f(T)} = 2\Gamma_n^{(T)}/\sigma_n^{0(T)}$. But the transverse crack length decreases when the coating strength increases from 0.05 to 0.10. This is related to the increase of the critical displacement $\delta_n^{0(T)} = \sigma_n^{0(T)}/k_n^{(T)}$. Therefore, with the increase of coating strength, the transverse crack length increases at first and then decreases. From Fig. 16(b), with the increase of coating fracture toughness, the transverse crack length decreases monotonously, and the displacement corresponding to initial cracking increases.

In contrast, the influences of parameters of interfacial cohesive elements on interface crack length are investigated for systems with a thick coating of $h_c/h_s = 0.4$, as shown in Fig. 17. Similarly, there exists a critical strength that changes the effect of interface strength on the crack evolution, while the effect of interface toughness is monotonous. The interfacial crack length increases when interfacial strength increases from 0.01 to 0.04, and then decreases as interfacial strength increases from 0.04 to 0.10, as Fig. 17(a) indicates. These are associated with the competition between the decrease of fracture displacement and the increase of critical displacement of the interface cohesive element. Fig. 17(b) illustrates that with increasing interfacial fracture toughness, the interfacial crack length decreases and cracking becomes difficult.

6. Conclusions

In this paper, the overall mechanical responses of single-material media and bi-material systems with cohesive elements are investigated by developing a series model theoretically and combining with the properties equivalence of the structure with cohesive zones. As cohesive elements are inserted into more complex systems, for instance, ceramic coating/substrate systems under three-point bending, the thickness-dependent damage and failure behaviors are characterized effectively by developing a FEM model.

When cohesive elements are inserted into single-material media, the equivalent elastic constants should be equal to those of the single-material media correspondingly before the softening stage of cohesive elements. Based on that, a selection criterion of stiffness of finite-thickness cohesive elements is proposed. Considering the whole process including the softening stage of cohesive elements, we obtain the overall stress-strain relationship and separation-strain relationship, both of which are just the functions of three dimensionless parameters: Λ, Λ_{cr} and σ_n^0/E_m. In the softening stage of cohesive elements, if the released elastic strain energy exceeds the increase of interface dissipation energy, the snap-back instability can be observed. Conversely, no snap-back behavior occurs and the system is stable.

When cohesive elements are inserted to interface of bi-material systems, considering the whole loading process, the overall mechanical responses including the stress-displacement relationship and separation-displacement relationship are obtained. The thickness-dependent failure characteristic on the macro scale is revealed both by theory and finite element simulations: with the increase of thickness of bi-material systems, the failure tends to be more catastrophic. This is associated with the increase of stored elastic strain energy as well as the releasing rate of elastic strain energy. And the failure characteristic is in accordance with molecular simulation results on the micro scale in previous literature.

For more complex systems like ceramic coating/substrate systems, cohesive elements are inserted into the coating and the interface simultaneously. The simulation results show the transition of dominated failure mode from coating cracking to interface delamination with the increase of coating thickness, which is validated by corresponding experiments. Damage evolution is further studied based on the power-law model, and the results show that the transition of dominated failure mode leads to faster damage of thick coating systems. Finally, the effects of interface toughness and strength of cohesive elements on failure of systems are revealed.

Acknowledgments

This work was supported by the National Natural Science Foundation of China (grant nos. 11672296, 91860102, 11372318, 11432014, 11672301, 11890681 and 11521202), and the Strategic Priority Research Program of the Chinese Academy of Sciences (grant no. XDB22040501).

Appendix A. The equivalence of Poisson's ratio and bulk modulus

Although the Poisson's ratio of cohesive elements denoted by ν_{CE} does not appear in bilinear traction-separation law, we can obtain its value from the analysis of deformation characteristics of cohesive elements. Actually, the lateral shrinkage of cohesive elements always follows that of the matrix material passively. In other words, the existence of cohesive elements does not affect the lateral shrinkage of the matrix material. Therefore, when the RVE is in uniaxial tension, the values of lateral shrinkage of cohesive elements, matrix material and the RVE are always the same, i.e., $\Delta H_{CE} = \Delta H_m = \Delta H$. Considering$E_m = k_n t_0$, we have

$$\nu_{CE} = -\frac{(\varepsilon_{yy})_{CE}}{(\varepsilon_{xx})_{CE}} = -\frac{\Delta H_{CE}/H}{\sigma_{xx}/(k_n t_0)} = -\frac{\Delta H_m/H}{\sigma_{xx}/E_m} = -\frac{(\varepsilon_{yy})_m}{(\varepsilon_{xx})_m} = \nu_m \tag{A.1}$$

Therefore, the Poisson's ratio of cohesive elements is proved to be equal to that of the matrix material.

Then, the equivalent Poisson's ratio of the RVE can be obtained. The normal strain of the RVE in the y direction can be expressed as

$$\varepsilon_{yy} = \frac{\Delta H}{H} = \frac{\Delta H_m}{H} = \frac{-\nu_m(\varepsilon_{xx})_m H}{H} = -\nu_m\frac{\sigma_{xx}}{E_m} = -\nu_{eq}\frac{\sigma_{xx}}{E_{eq}} \tag{A.2}$$

Consequently, we have

$$\nu_{eq} = \nu_m\frac{E_{eq}}{E_m} = \nu_m\frac{1 + t_0/L}{1 + E_m/(k_n L)} \tag{A.3}$$

It can be seen that $E_{eq} = E_m$ leads to $\nu_{eq} = \nu_m$.

On the other hand, the condition of $\nu_{eq} = \nu_m$ can be replaced by $K_{eq} = K_m$, where K_{eq} is the equivalent bulk modulus and K_m is the bulk modulus of matrix material. From the definition of bulk modulus, K_m is given by

$$K_m = \frac{(\sigma_0)_m}{\theta_m} = \frac{E_m}{3(1 - 2\nu_m)} \tag{A.4}$$

where $(\sigma_0)_m = \sigma_{ii}/3$ and $\theta_m = \Delta V_m/V_m = (\varepsilon_{ii})_m$ are the mean stress and volumetric strain of the matrix material. V_m is the volume of the matrix. The repeated indices i imply the Einstein summation convention and i ranges over x, y, z.

The non-zero strain components of the matrix material are $(\varepsilon_{xx})_m = \sigma_{xx}/E_m$ and $(\varepsilon_{yy})_m = (\varepsilon_{zz})_m = -\nu_m\sigma_{xx}/E_m$. The non-zero strain components of cohesive elements are $(\varepsilon_{xx})_{CE} = \sigma_{xx}/(k_n t_0)$ and $(\varepsilon_{yy})_{CE} = (\varepsilon_{zz})_{CE} = -\nu_{CE}\sigma_{xx}/(k_n t_0)$. It follows that the volume change of matrix material and cohesive elements, i.e., $\Delta V_m$and ΔV_{CE}, can

be expressed by

$$\begin{cases} \Delta V_{\mathrm{m}} = (\varepsilon_{ii})_{\mathrm{m}} V_{\mathrm{m}} = \dfrac{1-2\nu_{\mathrm{m}}}{E_{\mathrm{m}}}\sigma_{xx} \cdot (LBH) \\ \Delta V_{\mathrm{CE}} = (\varepsilon_{ii})_{\mathrm{CE}} V_{\mathrm{CE}} = \dfrac{1-2\nu_{\mathrm{CE}}}{k_{\mathrm{n}} t_0}\sigma_{xx} \cdot (t_0 BH) \end{cases} \tag{A.5}$$

Then, the volumetric strain of the RVE is

$$\theta = \frac{\Delta V}{V} = \frac{\Delta V_{\mathrm{m}} + \Delta V_{\mathrm{CE}}}{(L+t_0)BH} = \left(\frac{1-2\nu_{\mathrm{m}}}{E_{\mathrm{m}}}\frac{L}{L+t_0} + \frac{1-2\nu_{\mathrm{CE}}}{k_{\mathrm{n}} t_0}\frac{t_0}{L+t_0}\right)$$
$$\sigma_{xx} = \frac{\sigma_0}{K_{\mathrm{eq}}} \tag{A.6}$$

Noting that the mean stress is $\sigma_0 = \sigma_{ii}/3 = \sigma_{xx}/3$, the equivalent bulk modulus is given by

$$\frac{1}{K_{\mathrm{eq}}} = \frac{3(1-2\nu_{\mathrm{m}})}{E_{\mathrm{m}}}\frac{L}{L+t_0} + \frac{3(1-2\nu_{\mathrm{CE}})}{k_{\mathrm{n}} t_0}\frac{t_0}{L+t_0} \tag{A.7}$$

Substitution of Eqs. (8) and (A.3) in Eq. (A.7) yields

$$\frac{1}{K_{\mathrm{eq}}} = \frac{1}{K_{\mathrm{m}}} + \frac{6(\nu_{\mathrm{m}} - \nu_{\mathrm{CE}})}{E_{\mathrm{m}}}\frac{t_0}{L+t_0} \tag{A.8}$$

It can be seen that $K_{\mathrm{eq}} = K_{\mathrm{m}}$ requires $\nu_{\mathrm{CE}} = \nu_{\mathrm{m}}$ or $t_0 = 0$. Since $\nu_{\mathrm{CE}} = \nu_{\mathrm{m}}$ has been proved before, the equality of $K_{\mathrm{eq}} = K_{\mathrm{m}}$ is guaranteed whether t_0 is zero or not.

Appendix B. The power-law damage and catastrophic failure model

A brief introduction of the power-law damage and catastrophic failure model (Hao et al., 2013; Liang et al., 2016) is given as follows.

The damage variable of the system is defined by normalized transverse crack length: $D = l^{(\mathrm{T})}/l_{\mathrm{f}}^{(\mathrm{T})}$ (or normalized interfacial crack length: $D = l^{(\mathrm{I})}/l_{\mathrm{f}}^{(\mathrm{I})}$). The initial damage variable and the complete damage variable are $D_0 = l_0^{(\mathrm{T})}/l_{\mathrm{f}}^{(\mathrm{T})}$ (or $D_0 = l_0^{(\mathrm{I})}/l_{\mathrm{f}}^{(\mathrm{I})}$) and $D_{\mathrm{f}} = 1$, respectively. Subscripts 0 and f imply the damage initiation and complete failure, respectively. A controlling variable is defined by the normalized loading displacement: $\lambda = w/w_{\mathrm{f}}$. Similarly, the initial controlling variable and the complete controlling variable are given by $\lambda_0 = w_0/w_{\mathrm{f}}$ and $\lambda_{\mathrm{f}} = 1$, respectively. If the controlling variable is continuous and derivative for damage variable, it can be expressed as the Taylor expansion of the damage variable at the failure point:

$$\lambda = \lambda_{\mathrm{f}} + \frac{\mathrm{d}\lambda}{\mathrm{d}D}|_{D_{\mathrm{f}}}(D - D_{\mathrm{f}}) + \frac{1}{2}\frac{\mathrm{d}^2\lambda}{\mathrm{d}D^2}|_{D_{\mathrm{f}}}(D - D_{\mathrm{f}})^2 + o[(D - D_{\mathrm{f}})^2] \tag{B.1}$$

When it is close to the catastrophic failure point, the increasing rate of damage tends to infinity, i.e., $\lim_{\lambda \to \lambda_{\mathrm{f}}} \mathrm{d}D/\mathrm{d}\lambda = +\infty$. Substituting this relation into Eq. (B.1) and ignoring the terms that higher than the second-order, D can be expressed as (Liang et al., 2016):

$$D = 1 - C(1-\lambda)^{0.5} \tag{B.2}$$

where C is the damage coefficient. Considering when $\lambda = \lambda_0$, $D = D_0$, we can get the damage coefficient $C = (1 - D_0)/\sqrt{1-\lambda_0}$. From Eq. (B.2), we can know that the damage variable D with the controlling variable λ obeys the power-law relation with the exponent of 0.5.

The damage rate is given by (Liang et al., 2016)

$$R = \frac{\mathrm{d}D}{\mathrm{d}\lambda} = \frac{C}{2}(1-\lambda)^{-0.5} \tag{B.3}$$

It can be seen that the damage rate increases rapidly and has the singularity of order 0.5 near the catastrophic failure point. And the larger the damage rate or damage coefficient is, the faster the system damages.

References

Abanto-Bueno, J., Lambros, J., 2005. Experimental determination of cohesive failure properties of a photodegradable copolymer. Exp. Mech. 45, 144–152.

Abdul-Baqi, A., Van der Giessen, E., 2002. Numerical analysis of indentation-induced cracking of brittle coatings on ductile substrates. Int. J. Solids Struct. 39, 1427–1442.

Airoldi, A., Baldi, A., Bettini, P., Sala, G., 2015. Efficient modelling of forces and local strain evolution during delamination of composite laminates. Compos. Part B 72, 137–149.

Alfano, M., Furgiuele, F., Leonardi, A., Maletta, C., Paulino, G.H., 2008. Mode I fracture of adhesive joints using tailored cohesive zone models. Int. J. Fract. 157, 193–204.

Barenblatt, G.I., 1959. The formation of equilibrium cracks during brittle fracture. General ideas and hypotheses. Axially-symmetric cracks. J. Appl. Math. Mech. 23, 622–636.

Barenblatt, G.I., 1962. The mathematical theory of equilibrium cracks in brittle fracture. Adv. Appl. Mech. 7, 55–129.

Białas, M., Majerus, P., Herzog, R., Mróz, Z., 2005. Numerical simulation of segmentation cracking in thermal barrier coatings by means of cohesive zone elements. Mater. Sci. Eng. 412, 241–251.

Blal, N., Daridon, L., Monerie, Y., Pagano, S., 2012. Artificial compliance inherent to the intrinsic cohesive zone models: criteria and application to planar meshes. Int. J. Fract. 178, 71–83.

Camacho, G.T., Ortiz, M., 1996. Computational modelling of impact damage in brittle materials. Int. J. Solids. Struct. 33, 2899–2938.

Camanho, P.P., Davila, C.G., de Moura, M.F., 2003. Numerical simulation of mixed–mode progressive delamination in composite materials. J. Compos. Mater. 37, 1415–1438.

Cameselle-Molares, A., Vassilopoulos, A.P., Renart, J., Turon, A., Keller, T., 2018. Numerical simulation of two-dimensional in-plane crack propagation in FRP laminates. Compos. Struct. 200, 396–407.

Chaboche, J.L., Feyel, F., Monerie, Y., 2001. Interface debonding models: a viscous regularization with a limited rate dependency. Int. J. Solids. Struct. 38, 3127–3160.

Choi, S.T., Kim, K.S., 2007. Nanoscale planar field projections of atomic decohesion and slip in crystalline solids. Part I. A crack-tip cohesive zone. Philos. Mag. 87, 1889–1919.

Cui, W.C., Wisnom, M.R., Jones, M., 1992. A comparison of failure criteria to predict delamination of unidirectional glass epoxy specimens waisted through the thickness. Composites 23, 158–166.

Dassault Systèmes, 2014. ABAQUS 6.14 Analysis User's Guide.

Di Leo, C.V., Luk-Cyr, J., Liu, H., Loeffel, K., Al-Athel, K., Anand, L., 2014. A new methodology for characterizing traction-separation relations for interfacial delamination of thermal barrier coatings. Acta Mater. 71, 306–318.

Dugdale, D.S., 1960. Yielding of steel sheets containing slits. J. Mech. Phys. Solids 8, 100–104.

Falk, M.L., Needleman, A., Rice, J.R., 2001. A critical evaluation of cohesive zone models of dynamic fracture. J. Phys. IV 11 (PR5), 43–52.

Ferracin, T., Landis, C.M., Delannay, F., Pardoen, T., 2003. On the determination of the cohesive zone properties of an adhesive layer from the analysis of the wedge-peel test. Int. J. Solids. Struct. 40, 2889–2904.

Gall, K., Horstemeyer, M.F., Schilfgaarde, M.V., Baskes, M.I., 2000. Atomistic simulations on the tensile debonding of an aluminum–silicon interface. J. Mech. Phys. Solids 48, 2183–2212.

Gao, Y.F., Bower, A.F., 2004. A simple technique for avoiding convergence problems in finite element simulations of crack nucleation and growth on cohesive interfaces. Model. Simul. Mater. Sci. Eng. 12, 453–463.

Hamitouche, L., Tarfaoui, M., Vautrin, A., 2008. An interface debonding law subject to viscous regularization for avoiding instability: application to the delamination problems. Eng. Fract. Mech. 75, 3084–3100.

Hao, S.W., Rong, F., Lu, M.F., Wang, H.Y., Xia, M.F., Ke, F.J., Bai, Y.L., 2013. Power-law singularity as a possible catastrophe warning observed in rock experiments. Int. J. Rock Mech. Min. Sci. 60, 253–262.

Hao, S.W., Xia, M.F., Ke, F.J., Bai, Y.L., 2010. Evolution of localized damage zone in heterogeneous media. Int. J. Damage Mech. 19, 787–804.

Hertzberg, R.W., 1996. Deformation and Fracture Mechanics of Engineering Materials, fourth ed. John Wiley & Sons, Hoboken, NJ.

Klein, P.A., Foulk, J.W., Chen, E.P., Wimmer, S.A., Gao, H.J., 2001. Physics-based modeling of brittle fracture: cohesive formulations and the application of meshfree methods. Theor. Appl. Fract. Mech. 37, 99–166.

Kubair, D.V., Geubelle, P.H., 2003. Comparative analysis of extrinsic and intrinsic cohesive models of dynamic fracture. Int. J. Solids. Struct. 40, 3853–3868.

Kumar, D., Roy, R., Kweon, J.H., Choi, J.H., 2015. Numerical modeling of combined matrix cracking and delamination in composite laminates using cohesive elements Appl. Compos. Mater. 23, 397–419.

Lee, M.J., Cho, T.M., Kim, W.S., Lee, B.C., Lee, J.J., 2010. Determination of cohesive parameters for a mixed-mode cohesive zone model. Int. J. Adhes. Adhes. 30, 322–328.

Lelias, G., Paroissien, E., Lachaud, F., Morlier, J., Schwartz, S., Gavoille, C., 2015. An extended semi-analytical formulation for fast and reliable mode I/II stress analysis of adhesively bonded joints. Int. J. Solids. Struct. 62, 18–38.

Li, X.N., Liang, L.H., Xie, J.J., Chen, L., Wei, Y.G., 2014. Thickness-dependent fracture characteristics of ceramic coatings bonded on the alloy substrates. Surf. Coat. Technol. 258, 1039–1047.

Liang, L.H., Li, X.N., Liu, H.Y., Wang, Y.B., Wei, Y.G., 2016. Power-law characteristics

of damage and failure of ceramic coating systems under three-point bending. Surf. Coat. Technol. 285, 113–119.
Liang, L.H., Wei, H., Li, X.N., Wei, Y.G., 2013. Size-dependent interface adhesive energy and interface strength of nanostructured systems. Surf. Coat. Technol. 236, 525–530.
Needleman, A., 2014. Some issues in cohesive surface modeling. Procedia IUTAM 10, 221–246.
Neumayer, J., Koerber, H., Hinterhölzl, R., 2016. An explicit cohesive element combining cohesive failure of the adhesive and delamination failure in composite bonded joints. Compos. Struct. 146, 75–83.
Peng, S., Wei, Y., 2016. On the influence of interfacial properties to the bending rigidity of layered structures. J. Mech. Phys. Solids 92, 278–296.
Rabiei, A., Evans, A.G., 2000. Failure mechanisms associated with the thermally grown oxide in plasma-sprayed thermal barrier coatings. Acta Mater. 48, 3963–3976.
Riks, E., 1979. An incremental approach to the solution of snapping and buckling problems. Int. J. Solids. Struct. 15, 529–551.
Sarrado, C., Leone, F.A., Turon, A., 2016. Finite-thickness cohesive elements for modeling thick adhesives. Eng. Fract. Mech. 168, 105–113.
Schellekens, J.C.J., de Borst, R., 1993. A non-linear finite element approach for the analysis of mode-I free edge delamination in composites. Int. J. Solids. Struct. 30, 1239–1253.
Shi, Y., Soutis, C., 2016. Modelling transverse matrix cracking and splitting of cross–ply composite laminates under four point bending. Theor. Appl. Fract. Mech. 83, 73–81.
Simonovski, I., Cizelj, L., 2013. Cohesive element approach to grain level modelling of intergranular cracking. Eng. Fract. Mech. 110, 364–377.
Távara, L., Mantič, V., Graciani, E., París, F., 2011. BEM analysis of crack onset and propagation along fiber-matrix interface under transverse tension using a linear elastic-brittle interface model. Eng. Anal. Bound. Elem. 35, 207–222.
Tabiei, A., Zhang, W., 2017. Cohesive element approach for dynamic crack propagation: artificial compliance and mesh dependency. Eng. Fract. Mech. 180, 23–42.
Tan, H., Liu, C., Huang, Y., Geubelle, P., 2005. The cohesive law for the particle/matrix interfaces in high explosives. J. Mech. Phys. Solids 53, 1892–1917.
Tomar, V., Zhai, J., Zhou, M., 2004. Bounds for element size in a variable stiffness cohesive finite element model. Int. J. Numer. Meth. Eng. 61, 1894–1920.
Turon, A., Dávila, C.G., Camanho, P.P., Costa, J., 2007. An engineering solution for mesh size effects in the simulation of delamination using cohesive zone models. Eng. Fract. Mech. 74, 1665–1682.
Tvergaard, V., 1990. Effect of fiber debonding in a whisker-reinforced metal. Mater. Sci. Eng. 125, 203–213.
Tvergaard, V., Hutchinson, J.W., 1992. The relation between crack-growth resistance and fracture process parameters in elastic plastic solids. J. Mech. Phys. Solids 40, 1377–1397.
Vocialta, M., Richart, N., Molinari, J.F., 2017. 3D dynamic fragmentation with parallel dynamic insertion of cohesive elements. Int. J. Numer. Method Eng 109, 1655–1678.
Wan, J., Zhou, M., Yang, X.S., Dai, C.Y., Zhang, Y., Mao, W.G., Lu, C., 2013. Fracture characteristics of freestanding 8wt% Y_2O_3–ZrO_2 coatings by single edge notched beam and Vickers indentation tests. Mater. Sci. Eng. 581, 140–144.
Xu, X.P., Needleman, A., 1993. Void nucleation by inclusion debonding in a crystal matrix. Model. Simul. Mater. Sci. Eng. 1, 111–132.
Xu, X.P., Needleman, A., 1994. Numerical simulations of fast crack growth in brittle solids. J. Mech. Phys. Solids 42, 1397–1434.
Yamakov, V., Saether, E., Phillips, D.R., Glaessgen, E.H., 2006. Molecular-dynamics simulation-based cohesive zone representation of intergranular fracture processes in aluminum. J. Mech. Phys. Solids 54, 1899–1928.
You, X.M., Liang, L.H., Wei, Y.G., 2018. The atomistic simulation study of Ag/MgO interface tension fracture. Comp. Mater. Sci. 142, 277–284.
Yu, H., Olsen, J.S., Olden, V., Alvaro, A., He, J., Zhang, Z., 2016. Viscous regularization for cohesive zone modeling under constant displacement: an application to hydrogen embrittlement simulation. Eng. Fract. Mech. 166, 23–42.
Zhang, Z., Chen, Y., 2015. A constrained intrinsic cohesive finite element method with little stiffness reduction for fracture simulation. Eng. Fract. Mech. 136, 213–225.
Zhu, W., Cai, M., Yang, L., Guo, J.W., Zhou, Y.C., Lu, C., 2015a. The effect of morphology of thermally grown oxide on the stress field in a turbine blade with thermal barrier coatings. Surf. Coat. Technol. 276, 160–167.
Zhu, W., Yang, L., Guo, J.W., Zhou, Y.C., Lu, C., 2014. Numerical study on interaction of surface cracking and interfacial delamination in thermal barrier coatings under tension. Appl. Surf. Sci. 315, 292–298.
Zhu, W., Yang, L., Guo, J.W., Zhou, Y.C., Lu, C., 2015b. Determination of interfacial adhesion energies of thermal barrier coatings by compression test combined with a cohesive zone finite element model. Int. J. Plast. 64, 76–87.
Zou, Z., Reid, S.R., Li, S., 2003. A continuum damage model for delaminations in laminated composites. J. Mech. Phys. Solids 51, 333–356.